Chair of Spacecraft Systems
TUM School of Engineering and Design
Technical University of Munich

Enhancing Satellite End-of-Life Management:

Designing Structures for Optimal Demisability and Compliance in Low Earth Orbit

Patrick Jäger

Thesis for the attainment of the academic degree

Bachelor of Science (B.Sc.)

at the TUM School of Engineering and Design of the Technical University of Munich.

Examiner:
Prof. Dr. Alessandro Golkar

Supervisor:
Rafael Iliasov

Submitted:
Munich, 04/09/2024

I hereby declare that this thesis is entirely the result of my own work except where otherwise indicated. I have only used the resources given in the list of references.

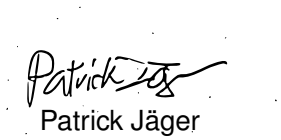

Munich, 04/09/2024 Patrick Jäger

Zusammenfassung

Das Zersetzen von Satelliten beim Wiedereintritt in die Atmosphäre ist noch immer ein viel diskutiertes Thema. Dieses bedarf weiterer Untersuchungen bezüglich der Übereinstimmung mit Weltraumschrottvermeidungsrichtlinien und internationalen Abkommen. Anhand der diesbezüglich entwickelten Struktur für einen 6U CubeSat, wurde das Verhalten neuer Materialien beim Wiedereintritt untersucht. Die Magnesiumlegierung WE43 eignet sich besonders, aufgrund ihrer mechanischen Kennwerte und der bisherigen Fortschritte in der Additiven Fertigung mit dieser Legierung. Außerdem veröffentlichten auch schon einige Forschungsgruppen Ergebnisse zu Analysen von Mikrogitter aus dieser Legierung. Die Eigenschaften der Struktur aus diesen Materialien wurden mit denen von der bereits etablierten Alumiumlegierung EN-AW 6082 verglichen. Für die Simulation der mechanischen Eigenschaften hat sich die Verwendung der Software Solidworks, als ein etabliertes Werkzeug, angeboten. Für die Simulation hat die ESA ihre Wiedereintrittssimulationssoftware DRAMA bereit gestellt. Hierbei hat sich die Legierung WE43 sowohl als volles Material, als auch in Form eines Mikrogitters als geeignet für die Verwendung in der Struktur von Satelliten herausgestellt. Das Wiedereintrittsverhalten von WE43 übertrifft das Verhalten von EN-AW 7075, bezüglich der Zersetzungsgeschwindigkeit.

Abstract

The demise of satellites is still an ongoing topic, that needs further investigation to comply with space debris mitigation guidelines and international agreements. Therefore a 6U CubeSat structure was designed to simulate the behaviour of new materials regarding their demisability. With advancements in the additive manufacturing of magnesium alloys the suitability of the rare earth alloy WE43 is investigated as solid material and in the structure of a micro lattice. The properties of these structures were compared to the structure made of aluminum EN-AW 6082. The used methods of simulation were Solidworks simulation for mechanical simulation and DRAMA for the demisability. It has been shown, that the WE43 is a suitable alloy for this use case and that the demise behaviour of WE43 exceeds the demise of the aluminum alloy EN-AW 7075.

Acknowledgements

I'm extremely grateful to my supervisor Rafael Iliasov for his support and advice during the time the of this thesis.
I also would like to express my deepest appreciation to Prof. Dr. Alessandro Golkar for the opportunity of this thesis.
Additionally, this endeavour would not have been possible, without the support of the ESA Space Debris Office, who provided me with access to valuable simulation tools and databases.

And i am also grateful for the support of the entire chair of spacecraft systems and every research assistant, that provided me with advice.
I also would like to extend my sincere thanks to Prof. Dr. Lothar Renke, Dr. Fabio Bothner, Roland Ort, Andreas Nicklas, Finn Kaus and Tim Burgtorf for the support and review of this thesis.

Lastly i want to thank my parents for their constant support.

Contents

List of Figures

List of Tables

List of abbreviations

LEO: Low earth orbit
CDS: CubeSat design specifications
EPS: Electrical power system
OBC: On-board computer
ADCS: Attitude determination and control system
OTV: Orbital transfer vehicle
OMV: Orbital maneuvering vehicle
WAAM: Wire arc additive manufacturing
PBF: Powder bed fusion

Constants

$h_l = 122km$ Altitude of the entry interface
$h_h = 2000km$ Upper border of Low earth orbit
$R_0 = 1m$
$R_\oplus = 6371km$ Radiusof the earth

List of symbols

E_{kin}: Kinetic energy
E_{pot}: Potential energy
E_{th}: Thermal energy
v_e: Entry velocity
g: Gravitational acceleration
h_u: Altitude

h_h: High edge of low earth orbit
q: specific heat
Q_w: Integral heat
C_f: Mean skin friction coefficient
C_d: Drag coefficient
m: Mass
Kn: Knudsen number
$\dot{q}_{S/C}$: Heat flux of the spacecraft
ρ_q: Sutton-Graves value of the heat transfer coefficient at the stagnation point
ρ: Air density
ρ_e: Mean atmospheric density
R_n: Radius of the surface curvature at the point where stagnation occurs
$\dot{q}_e$: Standard heat flux at entry interface
v: Velocity of the spacecraft
$v_\triangleright = 7.905 \frac{km}{s}$: First cosmic velocity
$St \approx 0.1\%$: Stanton number quantifying convective heat flux.
h_crit: Altitude of critical deceleration
H: Average scale height for the entire homosphere
κ_D: Reduced drag coefficient
γ_e: Flight path angle
a_{crit}: Critical deceleration
$v_{max\dot{q}}$: Velocity at the maximum heat flux
$\dot{q}_{S/Cmax}$: Maximum heat flux of the spacecraft

T_{max}: Maximum temperature
T_e: Entry temperature
B: Ballistic coefficient
E : Youngs modulus
ρ: Density
μ: Poisson's ratio
C: Specific heat capacity at 100℃
R_e: Yield strength
b: Number of bars
j: Number of joints
s: Number of independent states of self stress
q: Number of infinitesimal mechanisms of the framework
E_m: Youngs modulus of the micro lattice
P: Total external force
S: Cross-section area of whole micro lattice
F_i: Force for a certain strut
θ_i: Inclined angle for a certain strut
E_S: Young's modulus of the parent material
A: Cross-sectional area of a inclined strut
I: Moment of inertia of a strut
$EPSX$: Normal strain in the X-direction of the selected reference geometry
$EPSY$: Normal strain in the Y-direction of the selected reference geometry
$EPSZ$: Normal strain in the Z-direction of the selected reference geometry
$GMXY$: Shear strain in the Y-direction of the YZ-plane of the selected reference geometry
$GMXZ$: Shear strain in the Z-direction of the YZ-plane of the selected reference geometry
$GMYZ$: Shear strain in the Z-direction of the XZ-plane of the selected reference geometry
σ_{max}: Maximum stress

1 Introduction

The Kessler syndrome, as described by Donald J. Kessler and Burton G. Cour-Palais in 1978, predicts an exponential growth of satellite debris in Earth's orbit.The resulting accumulation of debris in Low Earth Orbit (LEO) compromises current and future space missions. This is detrimental and therefore has to be prevented [20].
The United Nations Office for Outer Space Affairs published their Space Debris Mitigation Guidelines of the Committee on the Peaceful Uses of Outer Space in 2010 with the newest version being released 2018 [8]. In accordance to those guidelines the U.S. Government [9] released in 2019 and the European Space Agency in 2023 [11] the newest version of their own guidelines on mission and spacecraft design, to mitigate the further space debris pollution.These guidelines propose two primary methods for satellite disposal: either maneuvering up out of LEO at the end of their operational life and by parking them in a graveyard orbit, or a heliocentric orbit outside of the earths gravitational field, or they have to be disposed by deorbiting to earth and burn up in the atmosphere.

In response to these regulations various methods have been suggested, the preferred method for most satellites in LEO is descend after their operational life-time. There are three possibilities of descending and demising a spacecraft, active descent, passive descent or by a mission altitude low enough, for the spacecraft to descent because of air resistance over the mission life-time [33].
Regardless of the method initiating the descent, the satellite has to comply to safety regulations. If the probability of casualties can not be prevented, this has to be addressed.
Risk management is one of the main topics of reentry disposal. How can the risk of casualties on the ground through reentry disposal be minimized? The regulations state that the risk of casualties on-ground must be lower than 10^{-4} in case of uncontrolled re-entry [11].
But to comply to this regulation it is fundamental that the least mass possible reaches the ground, so in the optimal and desired case every component of a satellite burns up during reentry. The two parameters of a spacecrafts structure that influence the demisability are the geometrical form of the spacecraft and the materials used.

This work investigates the usage of magnesium alloys and additive manufactured micro lattices of those magnesium alloys, comparing them to traditionally manufactured aluminum alloy structures. Therefore a 6U-CubeSat structure was designed and simulated in Solidworks with the goal to produce a flight ready structure. Furthermore different materials were simulated with DRAMA to compare the demisability.

2 CubeSats: An Overview

2.1 What are CubeSats?

CubeSats are a small satellite concept developed by Jordi Puig-Suari, Clark Turner and Robert Twiggs in a combined effort of California Polytechnic State University and Stanford University. This first had the objective to function for educational purposes, but quickly evolved into a suitable platform for science projects through their low cost and simplified construction compared to big satellites.[26]
Today CubeSats are used for education, science and commercial applications mainly in Low Earth Orbit not only because of their cost advantage, but also because of the short development time [25].
CubeSats are categorized either as a type of Nano or Micro spacecrafts depending on their size.

2.2 CubeSat Standardization and Sizes

The CubeSat Design Specification (CDS) published by the California Polytechnic State University is the standard document for CubeSats. This standard defines the dimensions of a CubeSat class, the required tests and specifications regarding mechanical, electrical and operational aspects. CubeSat classes are defined in the size unit U, there are 1U, 1.5U, 2U, 3U, 6U and 12U CubeSats. Relatively new are the CubeSat form factors 16U, 24U and 27U, although those are not defined explicitly defined in the CubeSat Design Specification Rev14.1. [17]
This standardization brings a lot of advantages. Compliance with the CDS reduces the amount of tests a satellite has to pass before launching it into the orbit. Also this standardization enabled a new commercial sector for off-the-shelf solutions for basic CubeSat components like the mechanical structure, the Electrical Power System (EPS), the On-Board Computer (OBC) and the Attitude Determination and Control System (ADCS). Also data collected about the behaviour of a CubeSat is more comparable. Figure 2.1 shows the different CubeSat sizes in comparison. The 1U CubeSat as the basic cubic unit possesses the dimensions of a Cube with a $10cm$ edge.

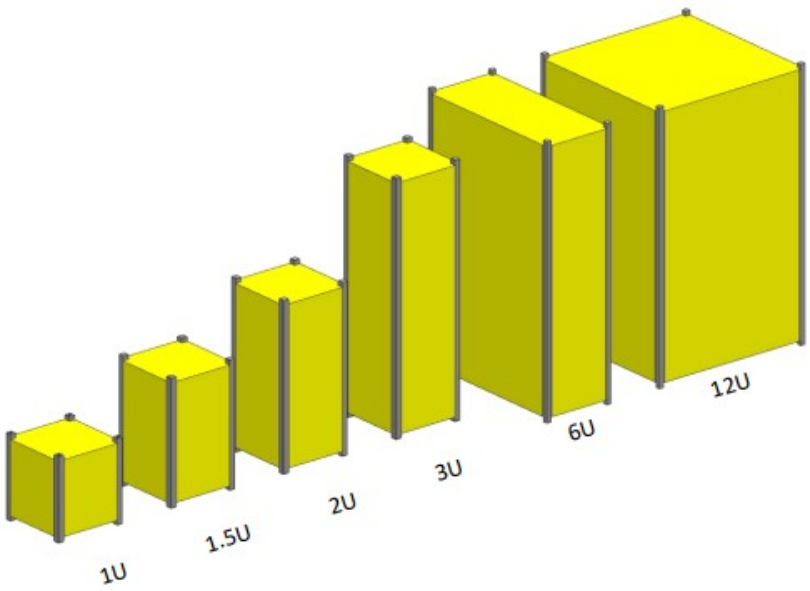

Figure 2.1 CubeSat size overview defined by CDS [17]

2.3 CubeSat Design and Components

A CubeSat is a system that consists of several subsystems. First of all the mechanical structure supports and protects the components that are attached to it. It can also have thermal or electrical functions but those can also utilise seperate components or can be integrated into other components. The Energysystem or Electrical Power System (EPS) is responsible for generating, storing and distributing electrical power and usually does this with Solar Panels, a batteries and Power Distribution Module. The Control of the CubeSat is handled by the OBC, the On-Board Computer that also processes all the data that is collected. The orientation also has to be maintained and this is done by the Attitude Determination and Control System(ADCS) that is in is simplest form a very sensitive magnetic instrument that has multiple reaction wheels to re-orientate the satellite in the magnetic field of the earth. Furthermore the Thermal system, regulates the temperature of the satellite to keep every Component in the proper operational temperature range. This is especially relevant in orbits that are not sun synchronous because of the very large temperature differences that satellites experience during their operational lifetime. A CubeSat also needs a communication system to transmit and receive data to and from mission control, which is the last necessary subsystem besides the payload. [12]

Commonly the material selected for a CubeSats mechanical structure is one of the aluminum alloys defined in the CDS [17]. But there has been an increased use of other materials. While Metals have generally homogeneous and isotropic properties, non-metallic materials are the opposite and can be used to withstand loads only in a specific direction. This decision requires information about the operational environment that the CubeSat is supposed to be in. Also with additive manufacturing there are new solutions for individual structures with materials that were not available before. For the structure there are two available approaches either the structure is custom designed and manufactured for the specific use case or the structure is a commercial off the shelf version. The custom structures can increase the efficient volume use, but have to be tested for compliance with all requirements and standards. The commercial structures are already tested and most of them have a flight heritage that proofs their function in space. [38]

2.4 CubeSat Mission Lifecycle

A CubeSat mission usually has multiple phases: Mission formulation, during which the general goal of the mission is formulated and contracts for funding and collaboration are closed; the requirement analysis phase where the mission requirements, the environmental requirements and the technical requirements are drafted and agreed upon. After that during the design phase, the subsystems are designed and tested and then put together in the integration phase.

2.5 CubeSat Deplyoment Methods

Currently the CubeSat either is deployed into its orbit with a CubeSat dispenser, from the ISS or with an Orbital Transfer / Maneuvering Vehicle (OTV/OMV). Deployment with a CubeSat dispenser is a critical part of every mission because there are many factors that determine if the CubeSat reaches its desired Orbit or not. A CubeSat dispenser is a metal case with a spring mechanism that shoots out the CubeSat once it gets the signal. The CubeSat dispenser also functions as an interface between the CubeSat and the launch vehicle and is therefore an important part of the development of the satellite. The separation from the launch vehicle is a critical part of the mission and there is no real benefit in developing an individual dispenser. There are various commercial vendors for CubeSat dispensers and through the defined dimensions of CubeSats, the off-the shelf version is the most common step. For deployment from the ISS a Nanorack ISS CubeSat Deployer is used. Hereby the CubeSat transported to the ISS in a pressurized vehicle is then mounted into the Nanorack ISS CubeSat Deployer and moved outside through the Kibo

Module's airlock. The CubeSat then sits also inside a metal case like a dispenser and is shot out in the right angle. The OTV/OMV methods are used when the primary payload of a rideshare has a different destination orbit than the CubeSat. Then the OTV/OMV can maneuver a CubeSat from an unpleasant Orbit to the desired one. OTVs and OMVs are relatively new with just very little flight heritage. The deployment method is a point that should be decided on early in the design phase because the interfaces need to be defined. [38]

2.6 CubeSat Cost Considerations

Satellite missions are very expensive projects. In Figure 2.2 the relative cost of a CubeSat 1U university project with a free launch provided by a space organization is depicted. Sometimes University projects get a free rideshare provided by a space organization like ESA or NASA to support the scientific community and allow students to get experience a real space project hands-on.
Also for the cost calculation since it is a model of a university project no salaries or similar for the design and construction is represented in the calculation.
In Figure 2.3 the relative Cost of a CubeSat 1U university project with a launch booked at SpaceX is depicted.
For the second mission the Launch cost are 45 000 USD/kg with a Falcon9 [28] and this results in about 6 times higher total cost than the first mission. Therefore the mass of the satellite is the biggest influence on the total project cost.
Table 2.1 shows the standard dimensions of the CubeSat Sizes up to 12U and the average mass of the mechanical structures available. This results in launch costs of about 40 000 USD alone.

Type	Dimension (mm)	Average Weight (kg)
1U	100x100x113.5	0.118
1.5U	100x100x170.2	0.142
2U	100x100x227	0.220
3U	100x100x340.5	0.352
6U	100x226.3x366	0.916
12U	226.3x226.3x366	1.84

Table 2.1 CubeSat Standard Structure Dimensions and Weight according to the 2023 State of the Art Small Spacecraft Technology Report[38]

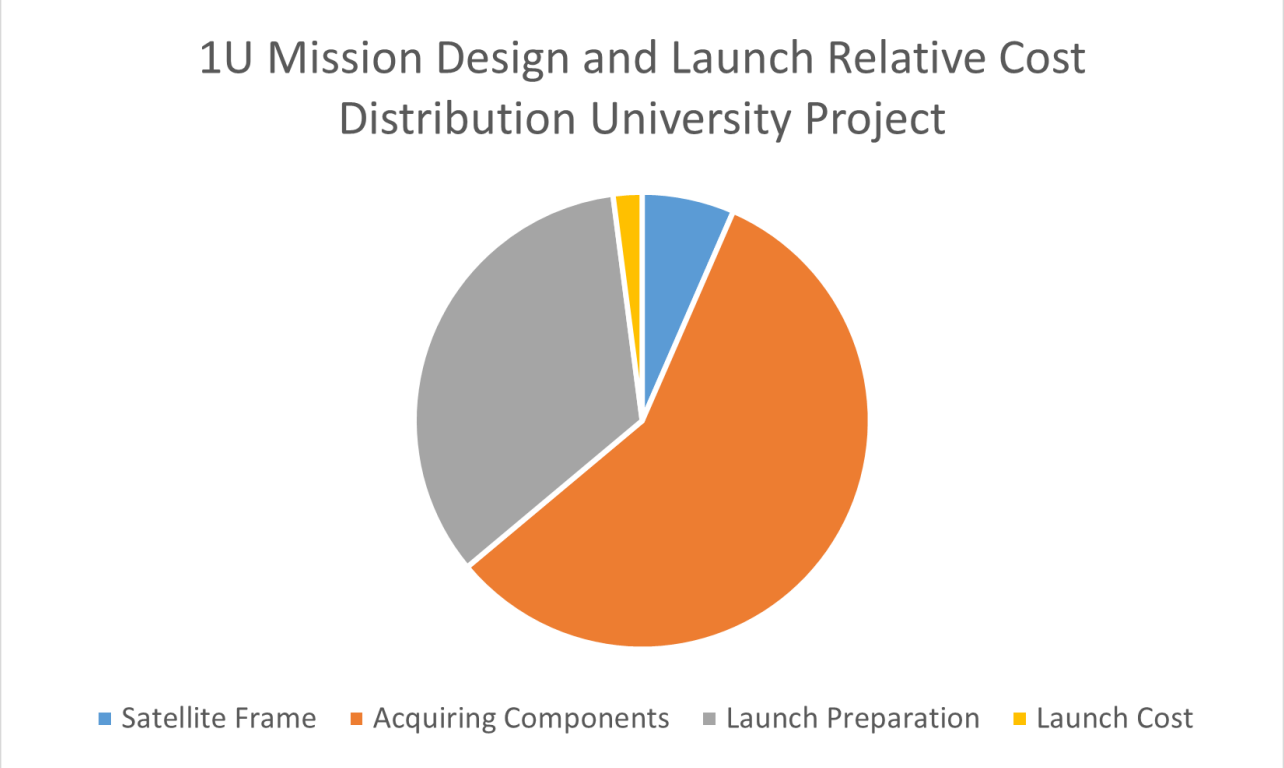

Figure 2.2 Relative Cost of a CubeSat 1U University project with free launch provided by a Space organization[7],[6]

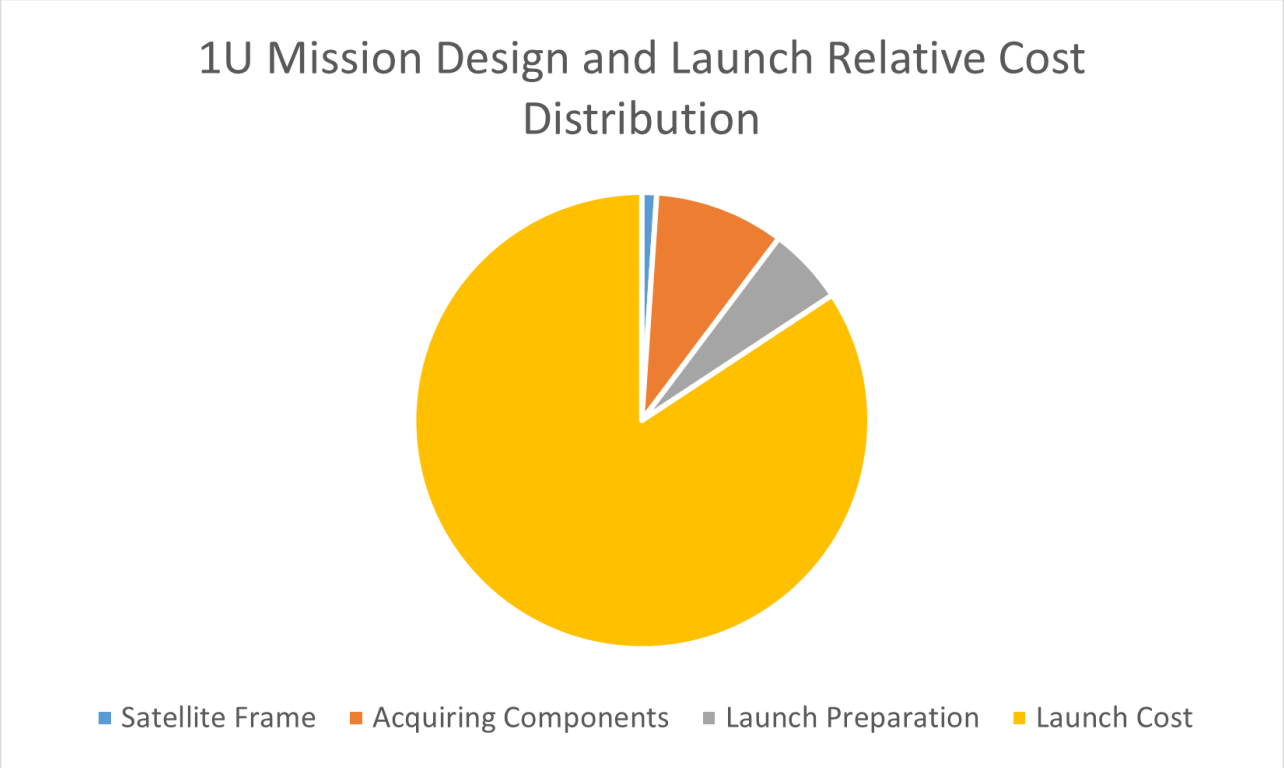

Figure 2.3 Relative Cost of a CubeSat 1U University project with a launch booked at SpaceX[7],[30], [6]

3 Debris Mitigation

3.1 Current Practises of Satellite Construction and Compliance with International Space Debris Agreements

The orbit around earth is constantly populated with little bodies and particles. These objects can be meteorites or micro meteorites of natural origin or artificial debris caused by space missions. The natural origin of space debris has an estimate total mass in LEO of around 200 kg, this is a result of periodically returning micrometeorite fluxes and sporadic fluxes. The natural space debris amount has only a little deviation over greater time periods and can be viewed as quasi-constant.
The artificial space debris on the other hand is accumulating through the rising human space activity. Everything that happens in space creates space debris, out-of-service satellites that stay in orbit or fragments of second stages of rockets or payloads come instantly to mind but also little objects like springs, bolts or blends of optical instruments become space debris. Solid fuel combustion creates micro particles. These are only a few examples of space debris sources. [12]
All these objects project a threat to all other objects in their region, because of the existing risk of collisions. These objects travel with very high velocities and one collision creates hundreds to tens of thousand new objects that each also travel with high velocities and rise the collision probability for the next collision. This effect like previously mentioned called the Kessler syndrom is first described by Donald J. Kessler and Burton G. Cour-Palais in 1978. They describe a point where a chain reaction starts causing exponential growth of space debris in LEO due to human space activities until the orbit is so densely populated, that no further spaceflight is possible. [20]
But there are also debris sinks that constantly create a negative debris flux in LEO. These are mainly the low air resistance that slows down objects gradually over time and the solar radiation pressure, both effects cause objects to leave their orbit and burn in earth atmosphere. [12]
There is still an ongoing discussion about what to do regarding the mitigation of space debris. Collecting the debris and removing it "by hand" would be an unmanageable effort. Two methods are currently applied, the mitigation of explosions on the orbit and the removal of satellites by deorbiting.

The process of deorbiting a satellite can either be done by an active maneuver or by passive deorbiting. Active deorbiting demands some sort of propulsion and therefore an engine. There are electrical or chemical engines that can be used for this purpose. The chemical propulsion method has a short burn time and a high mass flux and relatively low specific impulse. Therefore chemical engines need more fuel and therefore more mass, but with this short burn duration they enable Hohmann transfers which are very energy efficient. The electrical propulsion method has a very high specific impulse but a low mass flux and very long propulsion times, which causes them to spiral down over a long time duration while intersecting with other orbits which can create a higher collision risk.
Passive deorbit maneuvers have much longer deorbit times than active deorbit maneuvers. For passive deorbiting there is the method of using a big sail to slow down and deorbit that way. This method can only be used in the lower part of LEO because at a certain altitude there are simply not enough air particles left to cause a noticeable deceleration. Another passive method is the use of electromagnetic tethers that slow the spacecraft down using the magnetic field of the earth. There are various designs proposed for those magnetic tethers ranging form very long cables to components inside the satellite. The last method is releasing the spacecraft at an orbit that is not stable over the total mission lifetime and causes the spacecraft to deorbit by itself. The drawback of this method is that it can take a long time for the satellite to descent and during this process it intersects with many other orbits, what can cause a collision. [33]

3.2 Design for Demise

Previously the methods of deorbiting a spacecraft were discussed. But during spacecraft reentry there are many factors that determine if the spacecraft will be completely destroyed or if some parts survive and impact the ground. This carries a risk to the population on ground and therefore it is absolutely necessary to minimize that risk.

3.2.1 Design for Demise Techniques

Design for Demise is an approach to design a spacecraft, that complies with current demise regulations and minimizes casualty risks during reentry. There are different techniques of designing a spacecraft maximizing its demisability. First there is the method of reducing the heat load required to demise, this can be done by changing the material used, reducing the mass, changing the manufacturing, layering or segmentation of the component or designing for break-up at component level. The second method is the increase of the heat rate in order to demise the fragment. This includes designing components with a higher ballistic coefficient, increasing the break-up altitude, opening the structure, avoid that components shield each other from the heat flux, selection of the right attitude at re-entry time and the flight path angle.[10] But even by applying all the suggested methods above it is not guaranteed that the spacecraft will experience total demise and the re-entry environment cannot be tested on earth because of the power that would be necessary. But single Properties can be tested such as the destructive behaviour in the arc-heated supersonic wind tunnel like the one of the German Aerospace Center(DLR). There have already been tests of a complete nano-satellite and a reaction wheel by Rossi et Al. [27] in the context of the ReDSHIFT project. What they found was that aluminum structures are not very reliable regarding the demisability and strongly depend on the behaviour of the metal oxide layer. Furthermore this shows that especially the connections between the components are very critical for the demise process.[27]

3.2.2 Critical Components

Some components are typically harder to demise than others and in CubeSats the most critical components are the reaction wheels that are often part of the ADCS. The materials of those components, often titanium, have properties that make them hardly demisable. Those materials can not be changed because of their magnetic shielding capabilities. If simulations show that those components would survive until impact, a currently discussed solution is to contain all critical components in a separate container to decrease the casualty area during reentry.

In case of this work there are limited possibilities of application of most of the methods, except the choice of material and the mass reduction.

3.3 Reentry aerothermodynamics

In order to understand the behaviour of a spacecraft during reentry it is necessary to understand the environment and the thermodynamic and aerodynamic conditions the spacecraft is exposed to. The following section gives an overview of these conditions and the resulting relevant parameters for spacecraft demise. To evaluate if a structure can survive re-entry it is important to know the maximum stresses that occur. The critical parameters according to Walter [36] are:

1. Peak heat flux
2. Peak deceleration
3. Heat load
4. Peak dynamic pressure

Walter also states that the peak heat flux is an important parameter for material selection, heat load influences the chosen wall thickness. The peak deceleration and the peak aerodynamic pressure are two maximum stresses that occur and therefore influence the combination of material selection and geometry. A simple view on this matter is a plain use of the law of conservation of energy. A spacecraft possesses the kinetic energy E_{kin} and the potential energy E_{pot} at the beginning of its descent, with the potential reference level with no potential energy on earth's surface. According to the law of conservation of energy at the moment the spacecraft reaches the ground and the kinetic energy and the potential energy become 0, the total accumulated thermal energy E_{th} released in this process is (3.1)

$$E_{th} = E_{kin} + E_{pot} \tag{3.1}$$

If if the condition that the spacecraft will not impact the surface is applied the total energy is reduced to

$$E_{th} = E_{kin} + E_{pot0} - E_{pot1} \tag{3.2}$$

with E_{pot0} being the initial potential energy and E_{pot1} being the potential energy at the height of detonation or complete demise. To calculate the kinetic energy the orbital velocity equation (3.3) is used [12].

$$v_e = \sqrt{g \cdot (h_u + R_\oplus)} \approx \sqrt{g_h \cdot R_\oplus} \tag{3.3}$$

v_e: Entry velocity [$\frac{m}{s}$], g: Gravitational acceleration [$\frac{m}{s^2}$], h_u: Altitude [m], $R_\oplus$: Radius of earth [m]

LEO is defined as everything below the border altitude at $h_h = 2000km$, according to NASA. For re-entry the lower boundary is at the Entry Interface, which is according to Walter set at an altitude of $h_l = 122km$ at the border between heterosphere and homosphere. The orbital velocity for LEO ranges therefore between $\approx 7900\frac{m}{s}$ and $\approx 9000\frac{m}{s}$ for the LEO boundaries. [36]
With the orbital velocity the specific heat can be calculated [12].

$$q = \frac{1}{2}v_0^2 + g(h_0 - h_1) \tag{3.4}$$

By inserting our boundary values for v_e into equation (3.4) we obtain boundary values of $31.2\frac{MJ}{kg}$ and $40.5\frac{MJ}{kg}$ These are amounts of energy no solid material could withstand. For example Lithium with one of the highest specific heat capacities of $c_p \approx 3.5\frac{kJ}{kg \cdot K}$ would experience a temperature change of at least $\Delta T \approx 8900K$. If this were applicable there would be no reason for this thesis since a ballistic return to earth would be impossible.
However there are aerothermodynamic effects that transport heat away from a spacecraft during re-entry hence reducing the amount of total energy effecting the spacecraft. High temperature effects caused by particle collisions between the air and the spacecraft occur at the front of the spacecraft. These collisions are endothermic, causing a cooling effect on the gas in front of the spacecraft. Equation (3.5) is an approximation of the energy that impacts the surface temperature through friction.[12]

$$Q_w = \frac{1}{2}(\frac{C_t}{C_d}) \cdot \frac{1}{2}mv_e^2 \tag{3.5}$$

Q_w: integral heat, C_f: mean skin friction coefficient, C_d: Drag coefficient, m: mass

Friction resistance at turbulent boundary layers is approximately two to three times higher than at laminar boundary layers, therefore to maximize the heat flux the transition from laminar to turbulent flow should happen as soon as possible, which is another design parameter. There is no solution for a complete aerodynamic study of a spacecraft re-entry, hence the re-entry is divided into different phases during which different laws apply. These phases are the phase of free molecular stream, a transition phase and the continuum flow phase. The latter is defined by the Knudsen number $Kn \leq 0.01$. Directly in front of the spacecraft is the critical region where a nose shock causes the most extreme conditions. Depending on the temperature directly after the nose shock a variety of different effects may occur. [12]

1. Excitation of the molecules' vibrational degrees of freedom
2. Dissociation reactions of the oxygen and nitrogen molecules
3. Heat radiation of the gases
4. Ionisation of the air

The dissociation reactions of oxygen and nitrogen molecules can also lead to further release of heat energy, dependent on the surface properties of the spacecraft.This is the case for catalytic recombination reactions. The heat flux of a catalytic surface can be 50% higher than a non-catalytic surface.[12] This is incorporated in the Fay-Riddell equation for a cold wall (3.6)[13][4]

$$\dot{q}_{S/C} = \frac{St}{2}\sqrt{\rho\rho_q\frac{R_0}{R_n}}\cdot v^3 = \dot{q}_e\sqrt{\frac{\rho}{\rho_e}\frac{R_0}{R_n}}\cdot(\frac{v}{v_\triangleright})^3 \tag{3.6}$$

$\dot{q}_{S/C}$: heat flux of the spacecraft, ρ_q: Sutton-Graves value of the heat transfer coefficient at the stagnation point, ρ: air density, $R_0 = 1m$, ρ_e: mean atmospheric density, R_n: radius of the surface curvature at the point where stagnation occurs, $\dot{q}_e$: standard heat flux at entry interface, v: velocity of the spacecraft, $v_\triangleright = 7.905\frac{km}{s}$: first cosmic velocity, $St \approx 0.1\%$: Stanton number quantifying convective heat flux.

According to Walter through advanced one-dimensional adiabatic steady-state heat flux models made it possible to determine that the heat flux at the stagnation points of an aeroshell at hypersonic speeds is $\dot{q}_{S/C} \propto \sqrt{\frac{\rho}{R_n}}\cdot v^x$ with $x \approx 3$. It is further stated, that the result of this is that the heat flux at the stagnation point is maximal at $\frac{d\dot{q}}{d\rho} = 0$ at a given velocity $v = v(\rho)$. With this definition and the barometric formula, which applies for the homosphere, Walter derives the critical deceleration altitude h_{crit}.

$$h_{crit} = H\cdot\ln(\frac{2\kappa_D}{\sin\gamma_e}) \tag{3.7}$$

$H = 6.7 \pm 0.1km$: average scale height for the entire homosphere, κ_D: reduced drag coefficient, γ_e: flight path angle.
This is only the case for re-entry without lift. In the case of satellite structures, especially CubeSats the drag coefficient is higher than the lift coefficient resulting in no lift and therefore this equation and the following are very good approximations that provide the desired information. According to Walter the critical deceleration then is described by (3.8).

$$a_{crit} = (g_0 - \frac{v_e^2}{2eH})\cdot\sin\gamma_e \approx -\frac{v_e^2\cdot\sin\gamma_e}{2eH} \tag{3.8}$$

(3.9) describes the velocity at maximum heat flux.

$$v_{max\dot{q}} = \frac{v_e}{e^{\frac{1}{6}}} = 6.3\frac{km}{s}\cdot\sqrt{\epsilon_e} \approx 6.3\frac{km}{s} \tag{3.9}$$

(3.10) describes the altitude of the maximum heat flux.

$$h_{max\dot{q}} = H\cdot\ln\frac{6\kappa_D}{\sin\gamma_e} = h_{crit} + 1.1H \approx h_{crit} + 8.8km \tag{3.10}$$

This results in the following statement for the maximum heat flux of the spacecraft (3.11).

$$\dot{q}_{S/Cmax} = \frac{St}{2}\cdot v_e^3\sqrt{\frac{\rho_q\sin\gamma_e}{3eBH}\frac{R_0}{R_n}} = \dot{q}_e(\frac{v_e}{v_\triangleright})^3\sqrt{\frac{\sin\gamma_e}{3e\rho_eBH}\frac{R_0}{R_n}} \tag{3.11}$$

with $\dot{q}_e = 1.15\frac{W}{cm^2}$ as the standard heat flux at entry interface. Walter also mentions that the heat flux is reduced by a larger radius of curvature R_n and by a larger ballistic coefficient $B = C_D\frac{A_\perp}{m}$ The peak temperature is

$$T_{max}^4 = \frac{T_e^4}{\epsilon} \cdot (\frac{v_e}{v_\triangleright})^3 \sqrt{\frac{\sin\gamma_e}{3e\rho_e BH}\frac{R_0}{R_n}} \tag{3.12}$$

With these equations all the important parameters can be calculated.

4 Materials Comparison for CubeSat Structures

4.1 Introduction to CubeSat Materials

The material selection is an important part of the structural design, it defines the mechanical and thermal properties of the structure and therefore the maximum forces and moments that can be applied onto the structure without failure. Before using magnesium for the structure a comparison of the already in use aluminum alloys and the magnesium alloys that seem promising for aerospace applications is useful to estimate if these alloys can do the job in case of the mechanical loads and also to see what changes in the demisability behaviour can be expected.

4.2 Properties of Aluminum Alloys

The aluminum alloys commonly used for CubeSat structures are proposed by the CubeSat Design Specification and are EN-AW 5005, EN-AW 5052, EN-AW 6061, EN-AW 6082 and EN-AW 7075. That's why only this alloys are reviewed in this case. What makes aluminum alloys a very good materials for spacecraft structures in general is the low density compared to other material like steel and the still high young's modulus. Also the low procurement cost of aluminum and the good manufacturability makes it a very popular material. The detailed mechanical properties of the aluminum alloys are displayed in Table 4.1

	EN-AW 5005	EN-AW 5052	EN-AW 6061	EN-AW 6082	EN-AW 7075
Young's Modulus $E[GPa]$	70	71	70	70	72
Density $\rho[\frac{g}{cm^3}]$	2.7	2.68	2.7	2.7	2.81
Hardness, Vickers	-	-	-	95	68
Hardness, Brinell	28	47	30	-	60
Hardness, Knoop	-	-	-	-	68
Tensile Strength, Ultimate $[MPa]$	124	193	124	290	228
Tensile Strength, Yield $[MPa]$	41.4	89.6	55.2	250	103
Elongation at Break $[\%]$	25	30	25	10	10
Shear Strength$[MPa]$	75.8	124	82.7	179	152
Shear Modulus $[GPa]$	25.9	25.9	26	26	26.9
Poissons Ratio	0.33	0.33	0.33	0.33	0.33
Thermal Conductivity$[\frac{W}{m\cdot K}]$	200	138	180	170	173
Solidus$[K]$	905	880	885	853	750
Liquidus$[K]$	927	922	924	923	908

Table 4.1 Estimated Minimum Mechanical Properties of Wrought Aluminum alloys EN-AW-5005, EN-AW-5052, EN-AW-6061, EN-AW-6082 and EN-AW 7075[19], [14], [24]

What is clearly visible is that all of those alloys have about the same specific modulus which is specific modulus $= \frac{E}{\rho}$, but EN-AW 6082 far exceeds the other alloys regarding the tensile ultimate strength and tensile yield strength. Which makes this alloy especially suited for resisting higher mechanical loads.

4.3 Properties of Magnesium Alloys

Magnesium alloys have first of all the lowest density of any metal that can be used for structural applications, hence magnesium alloys are the best suited materials for lightweight structure design. While having this massive advantage in density they also tend to have a similar Young's modulus/density ratio as aluminum alloys shown in fig.:4.1. Furthermore especially the alloy WE43 shows dampening behaviour leading to energy dissipation, what is a huge advantage during launch because of the vibrational loads that occur. Regarding the demisability and thermochemical properties magnesium has a low melting point with the liquidus around 640 ℃. Magnesium also is a very reactive material, that quickly can enter combustion with a high combustion temperature, creating magnesium oxide gas. This combustion reaction is on earth difficult to extinguish because it does not require pure oxygen molecules, instead it can react with oxygen bound in other molecules like carbon dioxide with the reaction equation (4.1).

$$2Mg + CO_2 \longrightarrow 2MgO + C + energy \tag{4.1}$$

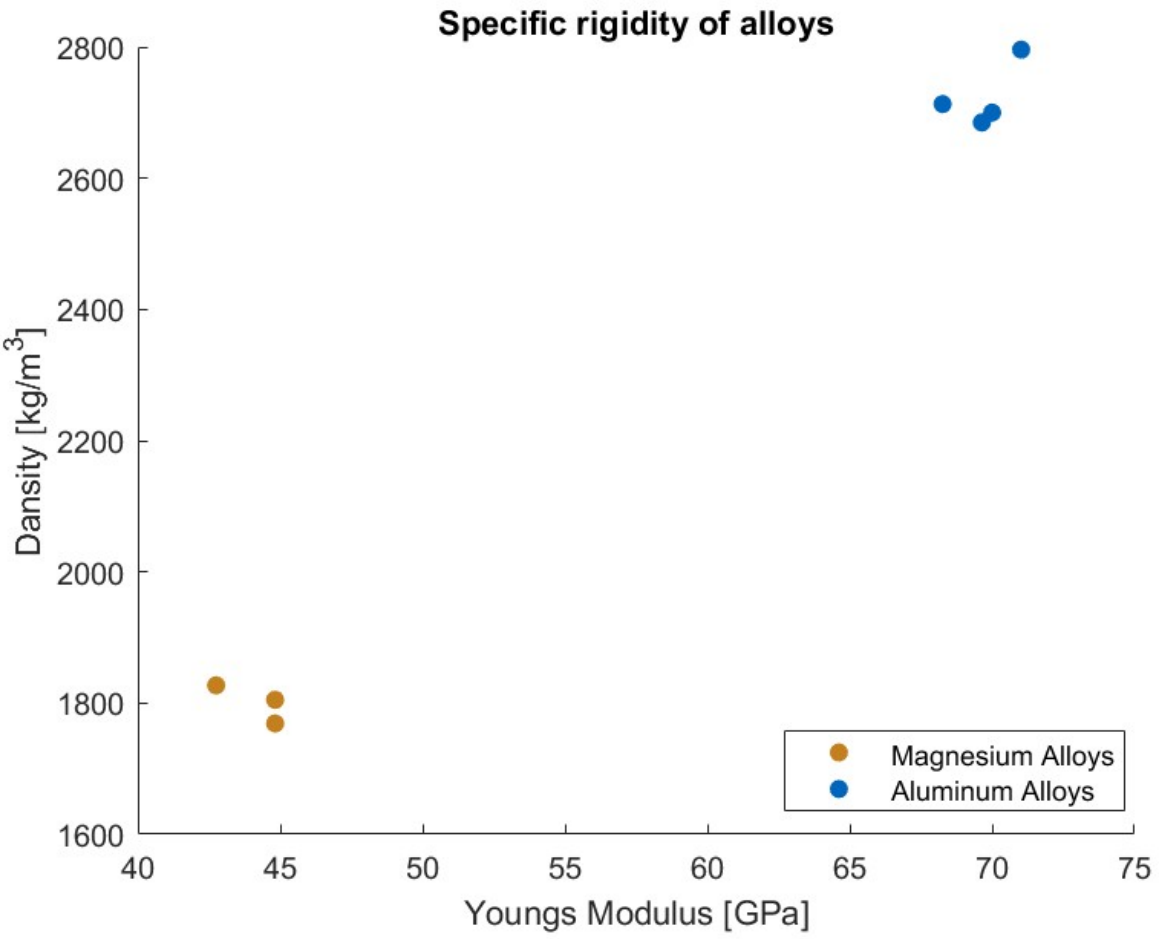

Figure 4.1 Density over Youngs modulus (specific rigidity) of aluminum alloys (blue) and magnesium alloys(orange)

4.4 Manufacturing Process for Aluminum Alloys

Aluminum alloys show an unfavourable behaviour regarding additive manufacturing. This is a big focus point in the additive manufacturing scientific community because of the divers applications aluminum is used for.[1]

This bad behaviour results in the fact that at the moment traditional manufacturing methods have to be applied when using aluminum alloys.

4.5 Manufacturing Process for Magnesium Alloys

Magnesium has very good machinability, in fact it is the easiest of all structural materials to machine. There is a relative machinability unit that measures the amount of power required to remove $16cm^3$ of metal, which uses magnesium alloys as the base with a value of one. Aluminum alloys have the value 1.8 and steel for example 6.3.[21]
The progress made on the field of additive manufacturing of metals also transfers slowly to magnesium alloys. The difficulty of this technique is that magneium has to be processed under inert conditions due to its reactive behaviour with oxygen.
Additive Manufacturing reshapes the whole building process of structures. It allows engineers to design structures with high detail without skyrocketing the cost of a part like it would with traditional manufacturing methods, resulting in lightweight parts that still have the mechanical properties necessary. As mentioned by Karunakaran et Al. there are multiple technologies for additive manufacturing of magnesium alloys that are tested.

1. Powder bed fusion
2. Wire arc additive manufacturing
3. Friction stir additive manufacturing
4. Binder jetting
5. Paste extrusion deposition

Powder Bed Fusion

During the process of powder bed fusion a very thin layer of powder gets selectively heated to the melting point by a heat source usually a laser in selective laser powder bed fusion or an electron beam in electron powder bed fusion to melt on layer of the designed part. Then the part moves down the distance of the thickness of one layer and a new layer of powder is distributed. This process is repeated until the part as a whole is produced. This process has many different factors, that also influence the properties of the finished product. These factors are laser or heat source power, scanning speed and layer thickness.[18]

Wire Arc Additive Manufacturing

Wire arc additive manufacturing (WAAM) is a technique, where in contrast to powder bed fusion a wire is used as basic material supply. The tip of the wire is melted by an arc of plasma to create little fluid drops of molten magnesium alloy that are applied onto the surface of the structure in an inert environment. For the inert environment different inert gases are used, like in the process of inert welding. The wire is hereby fed and melted at a constant rate or in a pulsating mode. Important parameters that influence the target geometry and accuracy are the travel speed of the nozzel, the wire feed speed and the dwell time, meaning the time between layers are added on top of each other[3]. This process has the advantage of having very little waste material. With WAAM more dense parts can be manufactured compared to Powder bed fusion.[18]

Friction Stir Additive Manufacturing

In this process sheets of magnesium alloy are welded together with heat as a result of friction between a rotating tool and the sheet. Parts manufactured show very high strength and a high increase of ductility, but also have a problem with porosity.[18]

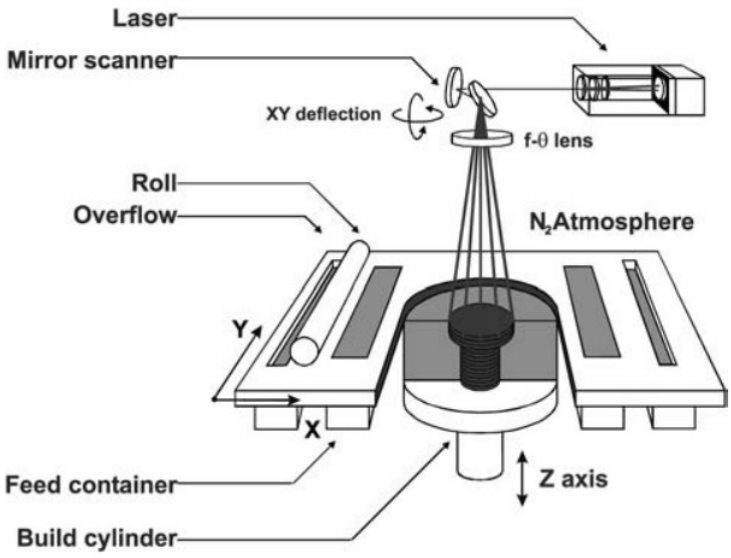

Figure 4.2 Schematic of a Powder bed fusion[22].

Binder Jetting

The process of binder jetting uses a powder bed as base material, just like the powder bed fusion. But instead of a heat source the particles are hold together by an ink that is selectively injected. This process is repeated layer for layer similar to the powder bed fusion. After every layer was injected with ink the powder bed is densified through sintering. Binder jetting has advantages over laser-based additive manufacturing in terms of cost per part and production speed. But those advantages are neglectable in the case of satellite structure production because of the low quantities.

Paste extrusion deposition can not achieve structurally strong parts and is mainly used for medical applications and therefore will not be discussed here.

Finishing

Finishing of magnesium alloy parts influences parameters like the hardness, the surface roughness and therefore also optical properties. The hardness does not really influence the material decision, since the only objects that would try to penetrate the material are travelling at high velocities and the hardness of a one layered one to three millimeter thick sheet does not provide enough protection for the internal parts. Hence the satellite has to avoid collisions regardless and the hardness of material therefore has no impact. One of the optical properties of the parts is the normal spectral reflectance and this property on the other hand does have a big impact on the demisability. Since the interaction of thermal radiation with matter is dependent on the reflectance ρ, the absorptance α and the transmittance τ with the relationship $1 = \rho + \alpha + \tau$, those parameters are important. Since $\tau = 0$ for opaque materials the lower the reflectance, the higher the absorptance and therefore the heatflux. The reflectance of Magnesium AZ-31B shown in fig.:4.3 indicates, that in infrared region the anodized materials generally have a lower reflectance, hence a higher absorptance than milled finishes.

4.6 Structural Properties Comparison

Both alloy groups, aluminum and magnesium show very good mechanical properties for use in space applications.

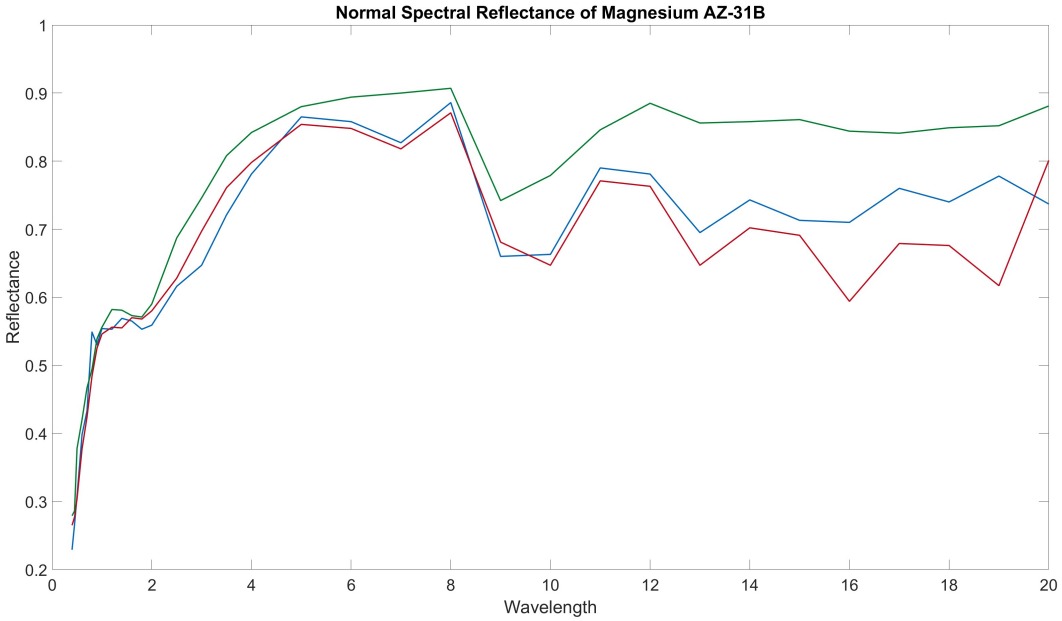

Figure 4.3 Normal Spectral Reflectance of Magnesium AZ-31B with different coatings [35]

Material	E [GPa]	ρ [$\frac{kg}{m^3}$]	μ	$C[\frac{J}{Kg \cdot K}]$	$R_e[MPa]$
Aluminum alloys					
EN-AW-5005	68.95				120
EN-AW-5052	69.64	2685	0.33	963	180
EN-AW-6061	68.26	2713	0.33	890	240
EN-AW-6082	70.0	2700	0.33	896	250
EN-AW-7075	71.02	2800	0.33	900	460
Magnesium alloys					
WE43-C	42.75	1827	0.295	1390	213
AZ91	44.82	1805	0.35	1047	190
AZ31B	44.82	1769	0.35	990	125

Table 4.2 Material properties of wrought aluminum and magnesium alloys[16]

E: Youngs modulus; ρ: Density; μ: Poisson's ratio; C: specific heat at 100℃; R_e: Yield strength

Tab.:4.2 shows the most important mechanical parameters for spacecraft design[37], furthermore the specific rigidity is shown in fig.:4.1. It is clearly visible that Magnesium alloys although having a lower density still has a comparable specific rigidity (density/Youngs modulus).This makes both alloy groups suitable for space applications.

4.7 Demisability Considerations

Demisability is influenced by various factors that cannot be recreated in a lab all at the same time, hence it is a not well researched topic. Most material demisability tests are done by looking at the melting of a material in an extremely hot air flux in a wind tunnel and these tests are expensive and just a small selection of materials have been tested to this conditions. There was no data found of testing results of the materials used in this work, so the behaviour has to be assumed based on tested material properties.

Alloy	EN-AW 7075	WE43
Density [$\frac{kg}{m^3}$]	2800	1840
Specific Heat @$333K$ [$\frac{J}{kg \cdot K}$]	893.5	1005
Melting Temperature [K]	850	866
Emission Coefficient [-]	0.4	0.35
Heat Conduction [$\frac{W}{m \cdot K}$]	163.89	51.3
Temperature of Ignition [K]	-	917
Heat of formation [$\frac{J}{kg}$]	-	-1.53E7

Table 4.3 Properties relevant for demise, comparison of two alloys[34][21][35][14]

Relevant properties are therefore the melting point, temperature of ignition and heat of oxide formation (if existing), density, specific heat, emission coefficient, heat conductivity, heat of fusion and the catalytic recombination coefficient for oxygen and nitrogen dissociation reactions. For last property also very little data was found. So according to this data shown in tab.:4.3 the aluminum alloy requires less energy to reach a certain temperature and has a lower melting point, both reduce the amount of energy needed for demise. Furthermore the aluminum alloy has a higher emission coefficient and therefore a higher absorption coefficient, meaning more thermal radiation of the high temperature gas can be absorbed during re-entry. But on the other side the magnesium has a much lower density, what results in less material that has to be demised and therefore less energy that is required. Also magnesium has a very active reaction with oxygen that is exothermic and sets a lot of heat free. This reaction behaviour could be a meaningful advantage of the magnesium alloy depending on the oxygen concentration in the atmosphere, when the structure reaches the ignition temperature.

4.8 Micro Lattice Structures

Micro lattice structures are organized porous structures with repeating unit cells. The unit cells are made out of very thin struts with strain diameters under 1mm. With the right choice of the lattice parameters very lightweight and stiff structures can be created, that even can have advantages like efficient insulation or cooling properties. [15] These structures are used in lightweight construction for various applications such as structural components in aerospace or automotive industries that require high strength-to-weight ratios, or biomedical implants.

There are various different unit cell types, that are tested in regard of their properties. Therefore the right choice of design and parameters is really important. Parameters can be for example unit cell diameter or strut diameter. Unit cell choice and choice of parameters both can influence the mechanical properties of the component on the macroscopic level by a lot. J. Clerk Maxwell shows that a frame consisting of only straight bars that are connected at their end by frictionless joints is stiff, when in the maxwell criterion that the frame consists of j joints and $3j - 6$ bars is met. It is still possible for frames lattice structures are classified in three categories regarding their rigidity, bending dominated, stretching dominated and static and kinematic determined. These categories are defined by the generalized Maxwell criterion (4.2). [5]

$$b - 3j + 6 = s - m \tag{4.2}$$

Where b is the number of struts,j is the number of joints, s is the number of independent states of self-stress and q is the number of infinitesimal mechanisms of the framework. If $s - m > 0$ then the structure is bending dominated and if $s - m < 0$ then the structure is stretching dominated. If $s = m = 0$ then the structure is static and kinematic determined. The Maxwell criterion is a necessary condition but it is not sufficient.[5] Bending dominated behaviour shows with a drop in stress after the maximum stress is achieved, which then stays on a plateau until densification in the region of the maximum strain. This behaviour is often desired since the total stress is kept constant. Stretch dominated behaviour occurs when continuous strain causes a oscillation of high and low stresses, which ends also in a densification in

the region of maximum strain. This behaviour is less useful for high loads, but it shows energy adsorption and energy dissipation effects that have other use-cases. [15]

Hyer et Al. [15] researched lattice structures produced with additive manufacturing of the magnesium alloy WE43. Six different lattice structures, shown in Figure 4.4 with four different parameter compositions were researched regarding their strength and density. The different lattices were tested in a compressive test. [15] The results with the highest specific strength to relative density ratio are shown in Table 4.4. This Ratio is the most relevant decision factor for light weight structures.

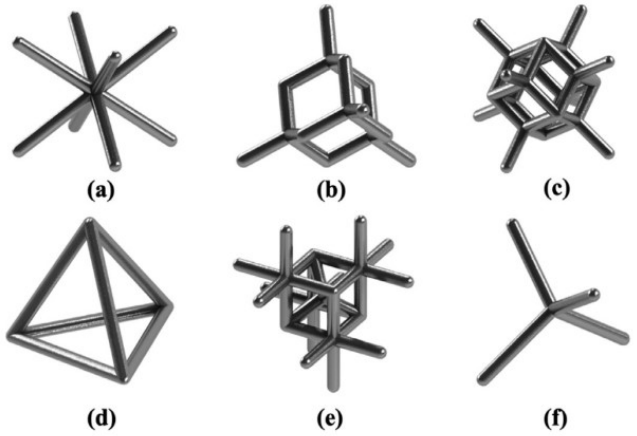

Figure 4.4 Unit Cells researched by Hyer et Al. (a) cubic vertex,(b) cubic diamond, (c) cubic fluorite, (d) tetrahedron octahedral edge, (e) tetrahedron octahedral vertex centroid, and (f) tetrahedron vertex centroid.

Unit Cell Type	d	n	relative density ρ_{rel}	specific strength (SpS)	$\frac{SpS}{\rho_{rel}}$
Cubic Vertex Centroid	0.75	10	0.24	6.27	26.13
Cubic Diamond	0.75	10	0.256	7.7	30.08
Cubic Fluorite	0.75	8	0.31	11.5	37.1
Cubic Fluorite	0.6	10	0.309	13.2	42.72
Cubic Fluorite	0.75	10	0.44	38.85	88.3
Tetrahedron Octahedral Vertex Centroid	0.6	8	0.188	6.35	33.78
Tetrahedron Octahedral Vertex Centroid	0.75	10	0.449	26.4	58.8

Table 4.4 Mechanical properties of different unit cell lattices made out of the magnesium alloy WE43 based on Hyer et Al. [15]

Song et Al. state that with some simplification that have to be done the Young's modulus of microlattices is (4.3). [29]

$$E_m = \frac{\Sigma\sigma_i}{\Sigma\epsilon_i} = \frac{P/S}{\Sigma\frac{F_i L \sin^2\theta_i}{E_S A} + \Sigma\frac{F_i L^3 \cos^2\theta_i}{12 E_S I}} \tag{4.3}$$

P is here the total external force, S is the cross-section area of whole microlattices, F_i is the force for a certain strut, θ_i is the inclined angle for a certain strut, E_S is the Young's modulus of the parent material, A is the cross-sectional area of a inclined strut, and I is the moment of inertia of a strut. With this equation the different Young's modulus of the different Lattices could be estimated.

For now the relevant information that we can derive is that cubic fluorite unit cell structures with a strut diameter $d = 0.75mm$ and a unit cell diameter of $3mm$ are verified as the best suited unit cell for resisting mechanical loads.

5 Structure Design

5.1 CubeSat mechanical Requirements

The mechanical Requirements for the 6U CubeSat were drafted from the CubeSat Design Spacifications (CDS). The values that are not defined in the CDS were either drafted from the Ariane 5 User Manual[23] or The Mission Success handbook for CubeSat missions by NASA [2]. In Ariane 5 User Manual it is postulated that the factor of safety, if not verified by test should always be 2.

1. Dimensions
   - 1.1 The dimensions shall be $366.0mmx226.3mmx100.0mm$
     Method of verification: Measurement with any suitable method of length determination.
   - 1.2 Rails shall have a minimum width of $8.5mm$ measured from the edge of the rail to the first protrusion on each face.
     Method of verification: Measurement with any suitable method of length determination.
   - 1.3 The edges of the rails should be rounded to a radius of at least $1mm$.
     Method of verification: Measurement with a template.
   - 1.4 The ends of the rails on the +/- Z face shall have a minimum surface area of $6.5mmx6.5mm$ contact area with neighboring CubeSat rails or the CubeSat dispenser.
     Method of verification: Measurement with any suitable method of length determination.
   - 1.5 The CubeSats center of mass shall fall within the ranges specified in table 5.1.
     Method of verification: Simulation.
2. Surfaces
   - 2.1 Any aluminum CubeSat external surfaces, such as rails and standoffs that are in contact with the dispenser rails, shall be hard anodized to prevent any cold welding within the dispenser.
     Method of verification: eddy current measuring.
   - 2.2 Rails should have a middle surface roughness less than $1.6\mu m$.
     Method of verification: Interferometer.
3. Testing
   - 3.1 Random Vibration
     - 3.1.1 The launcher interface diameter shall be $< 2624mm$.
       Method of verification: Measurement with suitable method of length determination
     - 3.1.2 The first fundamental lateral frequency shall be $> 10Hz$.
       Method of verification: Frequency simulation and random vibration tests.
     - 3.1.3 The first fundamental longitudinal frequency shall be $> 31Hz$. Method of verification: Frequency simulation, random vibration simulation and random vibration testing.
     - 3.1.4 No secondary mode shall be lower than the first primary mode. Method of verification: Frequency simulation, random vibration simulation and random vibration testing.
   - 3.2 Mechanical Loads
     - 3.2.1 The CubeSat shall withstand mechanical loads of $5g$ applied on all three axis at the same time. Method of verification: Static load analysis, Compression test. Acceptance value: Maximum stress at 5g*factor of safety < material strength.

3.3 Factors of safety (FoS)

3.3.1 The factor of safety shall always be 2 if the Property of interest is not verified by test.

4. Disposal

4.1 No fragment larger than $1cm^3$ of the CubeSat shall have an impact on the surface of the earth.

4.2 Bus components or payloads shall be mounted according to design for demise rules.

	X-Axis	Y-Axis	Z-Axis
6U	+4.5cm/-4.5cm	+2cm/-2cm	+7cm/-7cm

Table 5.1 Range of acceptable center of gravity locations as measured from the geometric center on each major axis of an 6U CubeSat

5.2 Design of the structure

In this chapter the design of the 6u CubeSat structure will be discussed and simulated to verify that the structural requirements are met.
Since this thesis also aims to compare the properties of additive manufactured structures with traditional manufacturing the structure is designed with the later use of additive manufacturing methods in mind and tries to limit the number of single parts.

5.2.1 Design parameters

The basic geometrical parameters for a 6U CubeSat structure are defined in the CubeSat Design Specifications [17]. The dimensions are $x = 226.3mm$, $y = 100mm$, $z = 366mm$ as shown in Figure 5.1. These mandatory geometrical parameters limit the possibilities of enhancing the geometrical structure in perspective of reentry disposal, but also give a very good starting point for the structural design. The approach for the design was to first look at the online publicly available information of designs of structures from multiple companies and compare their solutions for different problems. What was found is that their were modular approaches that can function in some sort of modular system and the components can be oriented in different directions and structures, that are completely reliant on their outer structure little internal support and where you can not change the orientation of the components.

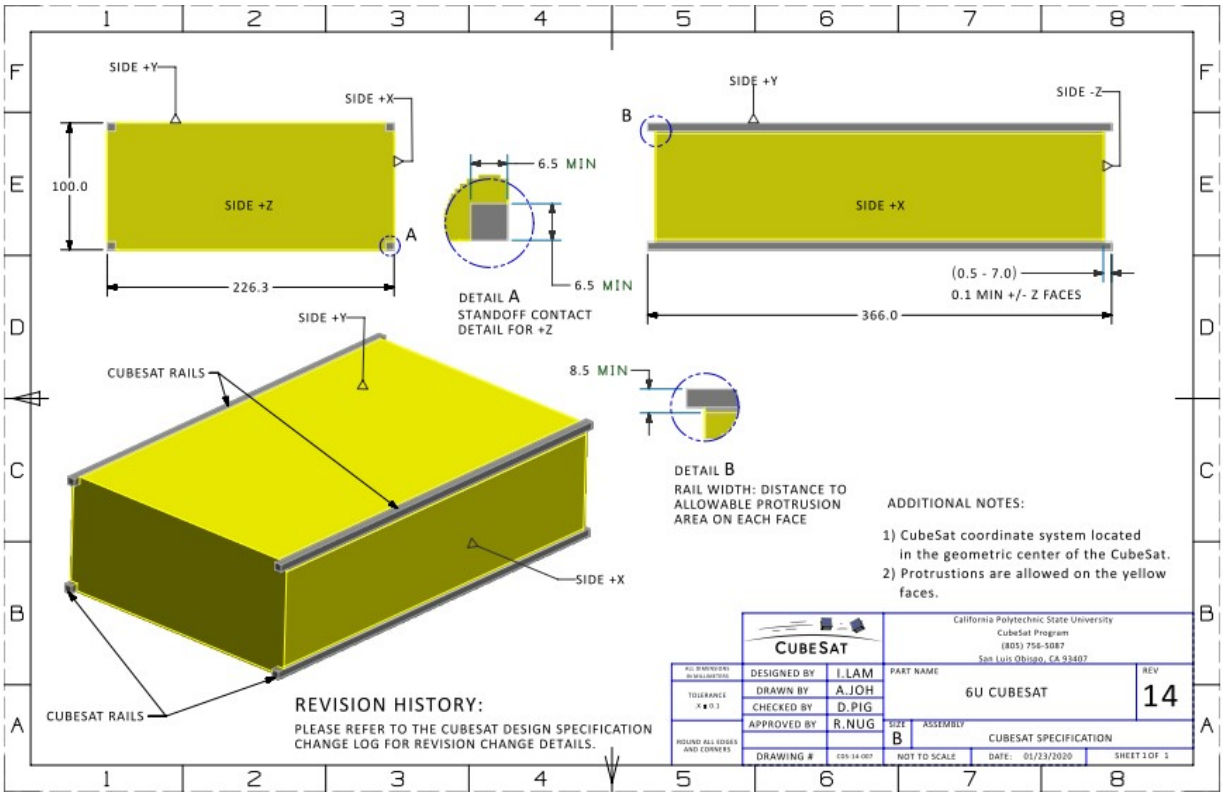

Figure 5.1 Dimensions of a 6U CubeSat defined by the CubeSat Design Specification from the California Polytechnic State University

The design of the structure is shown in Figure 5.2. This structure is designed with the use of additive manufacturing techniques in mind. Hence the number of parts was kept as low as necessary. There are 43 parts in this iteration of the construction with 26 of them being screws, 4 kill switches, 8 threaded rods, 1 internal component for vibration stabilisation, and 4 outer parts of the construction. The faces on the negative Y-side and on the positive and negative X-side are combined into one part. The single parts are visible in the explosion view in Figure 5.3.

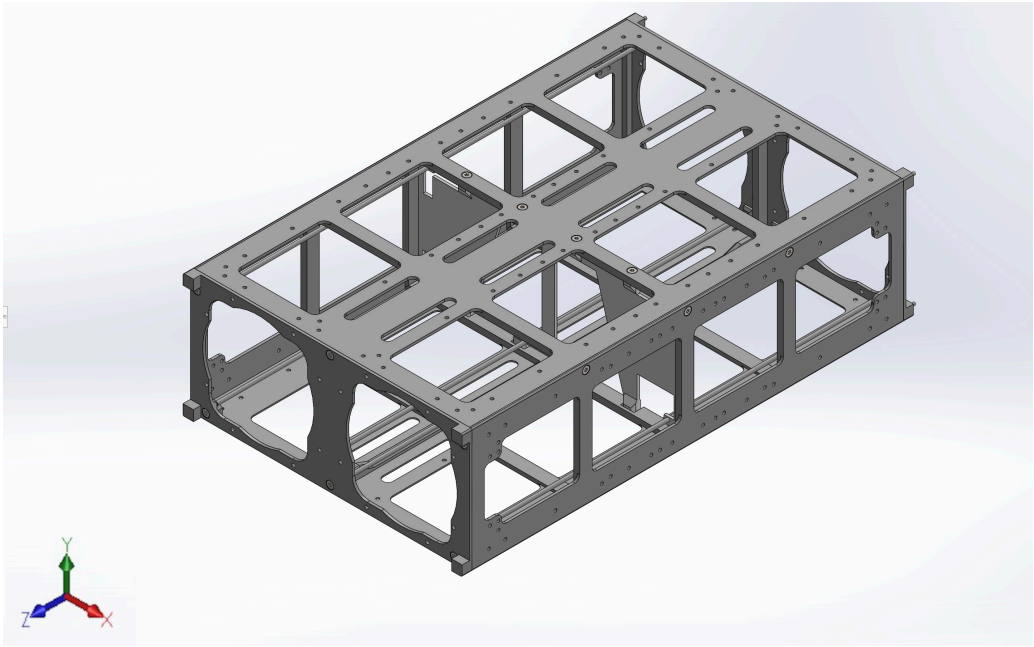

Figure 5.2 Display of the designed 6U CubeSat structure

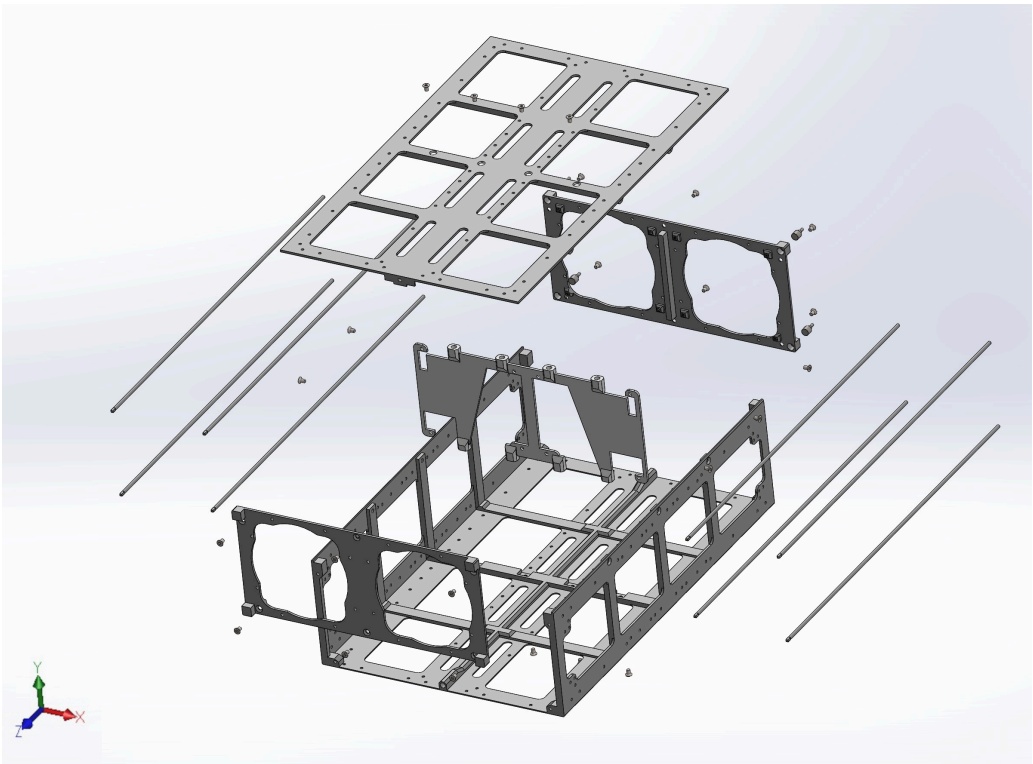

Figure 5.3 Explosion view of the 6U CubeSat structure

The same structure has different mass related properties, so in the following the mass related properties of the structure calculated from Solidworks are listed:
For the structure made of EN-AW 6082:

1. Mass
   $m = 951.26g$
2. Center of mass
   $$M = \begin{pmatrix} 0.027mm \\ -0.358mm \\ -1.167mm \end{pmatrix}$$
3. Main moment of inertia
   $$I = \begin{pmatrix} 7.91 & 0 & 0 \\ 0 & 13.83 & 0 \\ 0 & 0 & 18.43 \end{pmatrix} g \cdot m^2$$
4. Moment of inertia related to the output coordinate system
   $$L = \begin{pmatrix} 13.833 & -0.001 & 0.006 \\ -0.001 & 18.433 & 0.006 \\ 0.006 & 0.006 & 7.906 \end{pmatrix} g \cdot m^2$$

For the structure made of WE43 solid:

1. Mass
   $m = 667.73g$
2. Center of mass
   $$M = \begin{pmatrix} 0.026mm \\ -0.431mm \\ -1.734mm \end{pmatrix}$$
3. Main moment of inertia
   $$I = \begin{pmatrix} 5.531 & 0 & 0 \\ 0 & 9.712 & 0 \\ 0 & 0 & 12.928 \end{pmatrix} g \cdot m^2$$
4. Moment of inertia related to the output coordinate system
   $$L = \begin{pmatrix} 9.712 & -0.001 & 0.004 \\ -0.001 & 12.93 & 0.006 \\ 0.004 & 0.006 & 5.531 \end{pmatrix} g \cdot m^2$$

For the structure made of the WE43 micro lattice:

1. Mass
   $m = 192.48g$
2. Center of mass
   $$M = \begin{pmatrix} 0.06mm \\ -17.9mm \\ -6.58mm \end{pmatrix}$$

3. Main moment of inertia

$$I = \begin{pmatrix} 1.815 & 0 & 0 \\ 0 & 2.547 & 0 \\ 0 & 0 & 3.786 \end{pmatrix} g \cdot m^2$$

4. Moment of inertia related to the output coordinate system

$$L = \begin{pmatrix} 2.547 & -0.000 & 0.002 \\ -0.000 & 3.786 & -0.016 \\ 0.002 & -0.016 & 1.815 \end{pmatrix} g \cdot m^2$$

So the main difference is the lower total mass of the structure made of WE43, which is no surprise since it has a much lower density. But the resulting lower moment of inertia provides another simple advantage, requiring less force for the attitude determination and enabling more precision. On the other side the lower moment of inertia results in a lower resistance to tumbling.

5.3 Design of the Micro Lattice

It was not possible with the available computation resources to construct the 6U-structure with a micro lattice, since Solidworks has no build in implicit modelling function and with the traditional CAD-tools the resource demand to process a part that is build up with a micro lattice is just too high. Therefore a small micro lattice was designed in Solidworks following the description of Hyer et Al. [15].
This micro lattice component is a cube with the side length $a = 30mm$ and the chosen lattice structure was the tetrahedron octahedral edge design.
As shown in Figure 5.4 the probe was build in a sandwich structure to have a plain where test forces can be applied. Then the stress/strain curve of this lattice was approximated via multiple simulations. The stress/strain curves of the tested sample and the simulated one show no match what leads to the conclusion that there would have been further constraints to be determined for Solidworks to simulate the proper behaviour of a micro lattice.
So another approach was used, where the mechanical property results of the tests were used to define a new material in Solidworks with the macroscopic mechanical properties of a micro lattice. This approach neglects any internal failure that may occur through the interactions between the struts and the maximum stress that may occur if the force is not equally divided, but shows the macroscopic behaviour with the named drawbacks in mind.
Figure 5.5 shows the stress/strain plots of the Tetrahedron octahedral edge probe tested by Hyer et Al[15]. The stress behaviour shows that the probe experiences multiple stress spikes under pressure until the maximum strain is reached. This sawtooth behaviour can be explained with multiple events of deformation happening inside the structure according to Hyer et Al. Therefore when longterm use of micro lattice structures is intended, the first and largest maximum should not be reached.

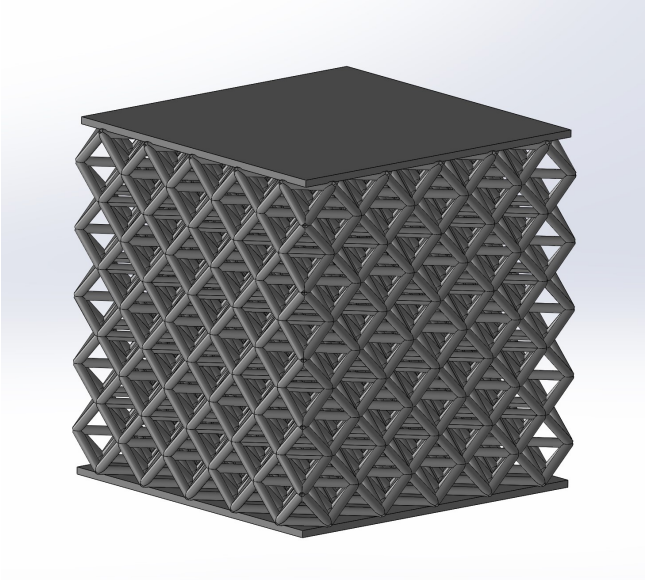

Figure 5.4 Tetrahedron octahedral edge probe sandwich structure modelled in Solidworks

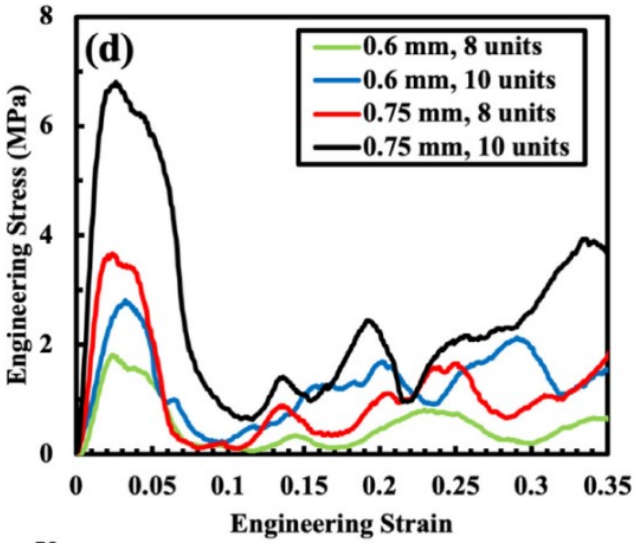

Figure 5.5 Stress-Strain diagram of the tetrahedron octahedral edge lattice testing results[15]

6 Mechanical Simulation

The Requirements for the mechanical structure that were previously discussed obviously have to be tested and verified. Since it would be expensive and time consuming to test the structure in every iteration of design, the simulation tools of Solidworks were used to get a theoretical impression of the structures mechanical properties.
The general approach was hereby to construct the structure with the material EN-AW 6082 and verify the fulfillment of the requirements via simulation, before adapting the structure to the properties of the magnesium alloy WE43. Because of the time the different simulations take the workflow depicted in Figure 6.1 was established and used. The static load analysis was always done with forces applied on one, two and three axis. Each of those simulations were done in a couple of minutes and were the quickest simulations. The longest time per simulation for the CubeSat structure was 15:30h for the non-linear forces simulation of the micro lattice.Important mechanical parameters are the occurring maximum Von-Mise stress, the maximum equivalent strain, the maximum displacement and the natural frequency. The Von-Mise stress is calculated in Solidworks by (6.1) with $\sigma_{vonMises} \geq \sigma_{limit}$, where σ_1, σ_2, σ_3 are the principal stresses in descending order [31].

$$\sigma_{vonMises} = \sqrt{\frac{(\sigma_1 - \sigma_2)^2 + (\sigma_2 - \sigma_3)^2 + (\sigma_1 - \sigma_3)^2}{2}} \tag{6.1}$$

The equivalent strain calculation is described in (6.2)

$$ESTRN = 2 \cdot \sqrt{\frac{\epsilon_1 + \epsilon_2}{3}} \tag{6.2}$$

where:

$$\epsilon_1 = 0.5 \cdot [(EPSX - \epsilon^*)^2 + (EPSY - \epsilon^*)^2 + (EPSZ - \epsilon^*)^2] \tag{6.3}$$

$$\epsilon_2 = \frac{(GMXY)^2 + (GMXZ)^2 + (GMYZ)^2}{4} \tag{6.4}$$

$$\epsilon^* = \frac{EPSX + EPSY + EPSZ}{3} \tag{6.5}$$

EPSX: Normal strain in the X-direction of the selected reference geometry.
EPSY: Normal strain in the Y-direction of the selected reference geometry.
EPSZ: Normal strain in the Z-direction of the selected reference geometry.
GMXY: Shear strain in the Y-direction in the YZ-plane of the selected reference geometry.
GMXZ: Shear strain in the Z-direction in the YZ-plane of the selected reference geometry.
GMYZ: Shear strain in the Z-direction in the XZ-plane of the selected reference geometry.
ESTRN: Equivalent strain.[32]

6.1 Static Load Analysis

Static load analysis calculated with the force of 1200N on each axis that it was applied. The resulting parameters are the Von-Mise stress, the strain and the displacement. The objective of the simulation was to test the structural integrity against the applied maximum loads times factor of safety defined in the requirements. The maximum resulting Von-Mise stress has to be lower than the material strength to

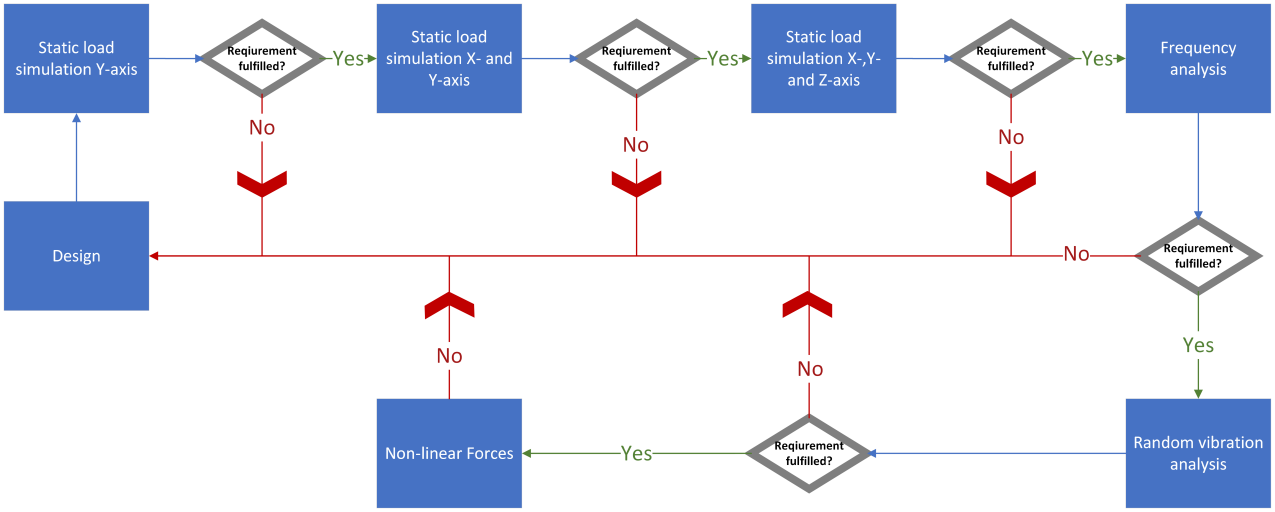

Figure 6.1 Mechanical Analysis Workflow

pass the test. The strength of EN-AW 6082 is $250MPa$ and the maximum Von-Mise stress simulated is $130MPa$. Therefore even higher loads are possible which enables the survival of combined loads.Figure 6.2 shows the simulation results for the stress with the defined load applied on the Y-axis in negative Y-direction. It is visible that the highest stresses occur in the regions around the screws. Reducing the amount of screws necessary therefore also should reduce the number of stress peaks and therefore the total probability of failure. The stress maximum is not visible in the picture, but it occurs in the lower corners of the structure on the inside, where the screws are. The strain and displacement results are shown in Figure A.1 and in Figure A.2. The same conditions as above apply. The largest displacement occurs at the top of the structure at the two places with the largest distance to a vertical support. The largest displacement is $\Delta l_max = 0.29mm$.
The WE43 analysis showed that it is a suitable material to be applied with this structure. The micro lattice made out of WE43 shows in Figure 6.4 a maximum occurring stress in the static load analysis of $\sigma_{max} = 161MPa$, this analysis was done with a factor of safety of 1.25 since the maximum occurring stress in the simulation with a factor of safety of 2 was $298MPa$ and therefore would be too high. This maximum stress only occurs at the bottom contact between the front and the bottom structure at one point. The failure of the structure can be prevented, by using a combination of 99% WE43 and the micro lattice at this point. The maximum strain shown in Figure A.5 is also in an acceptable range. The maximum displacement is with a value of $0.5mm$ just slightly higher than the maximum displacement of the EN-AW 6082 structure.

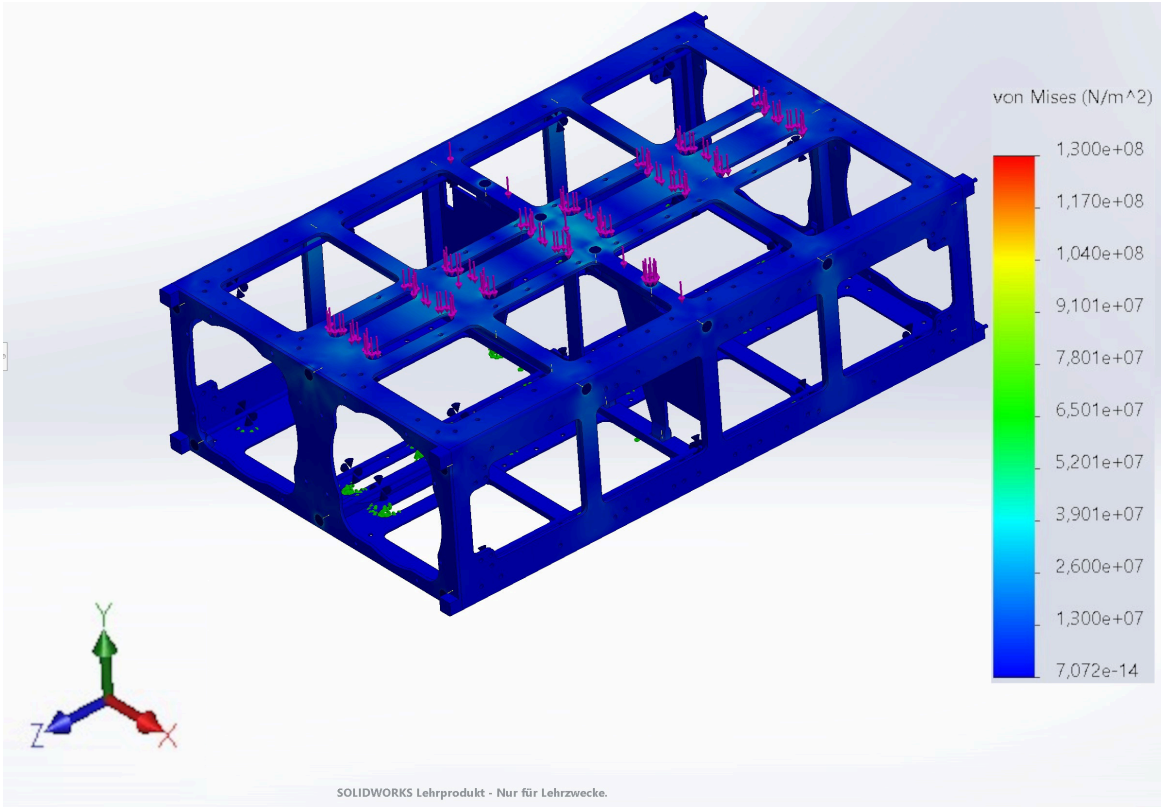

Figure 6.2 Mechanical stress results of the static load analysis of the 6U CubeSat structure made out of EN-AW 6082 with a force of 1200N applied in negative Y-direction

In comparison to the structure made of EN-AW 6082 the WE43 structure shows in Figure 6.3 a maximum stress of $\sigma_{max} = 292.9MPa$ and in Figure A.3 the maximum strain is $4.302E-3$ and in Figure A.4 the maximum displacement is $0.869mm$

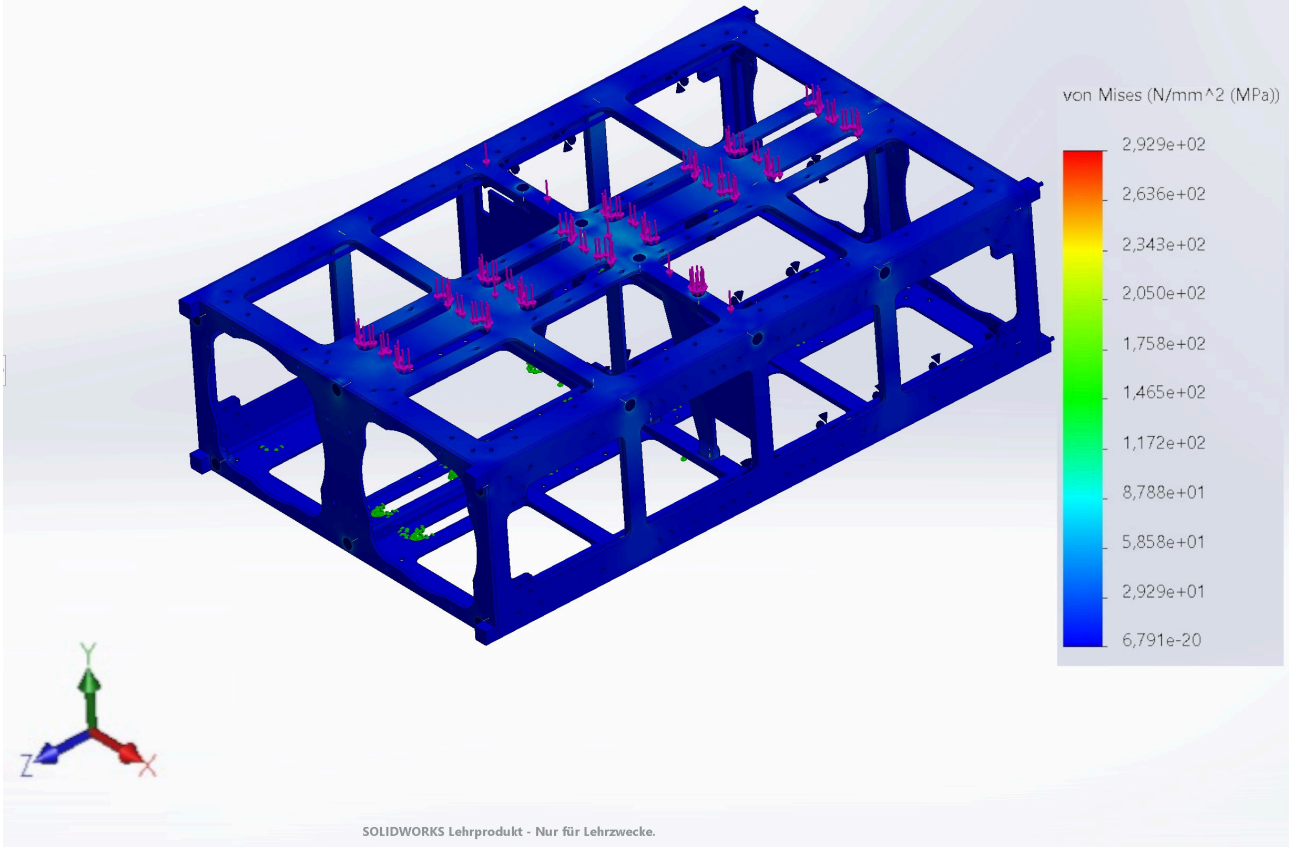

Figure 6.3 Mechanical stress results of the static load analysis of the 6U CubeSat structure made out of WE43 with a force of 1200N applied in negative Y-direction

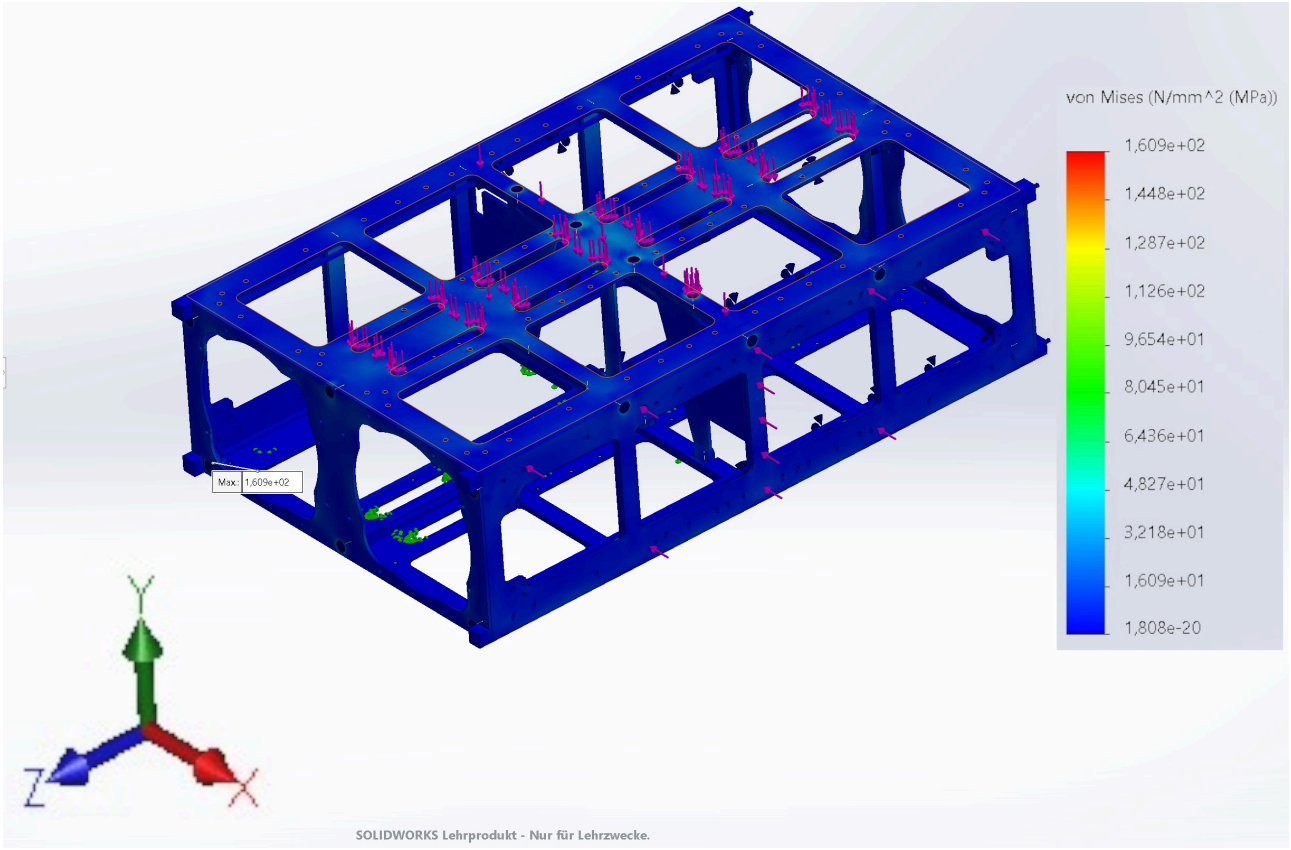

Figure 6.4 Mechanical stress results of the static load analysis of the 6U CubeSat structure made out of the WE43 micro lattice with a force of 1200N applied in negative Y-direction

6.2 Frequency Analysis

The next analysis is the frequency analysis, that calculates the modes of vibration and the corresponding natural frequencies. The first natural frequency is here of especial interest since it is the lowest natural frequency. Launch vehicles typically induce vibrations at very low frequencies, for example the Ariane5 rocket induces vibrations up to $31Hz$. To prevent dynamic coupling that can lead to critical failure the first natural frequency is required to be over this threshold. Figure 6.5 shows the first mode of the structure with natural frequency $f_0 = 293.8Hz$.
The Analysis of the WE43 structure shows a similar first natural frequency as the EN-AW6082 structure. The first mode of the WE43 structure is displayed in Figure 6.6. The study shows in Figure 6.7, that the structure made out of the micro lattice has a first natural frequency of $f_0 = 293Hz$ and therefore fulfills the requirement.
What is interesting that although the first natural frequency is about the same, the first mode of the aluminum alloy structure has a completely different mode shape in the analysis, than the other structures. The deformation happens at the top face instead and not on one of the rods inside.

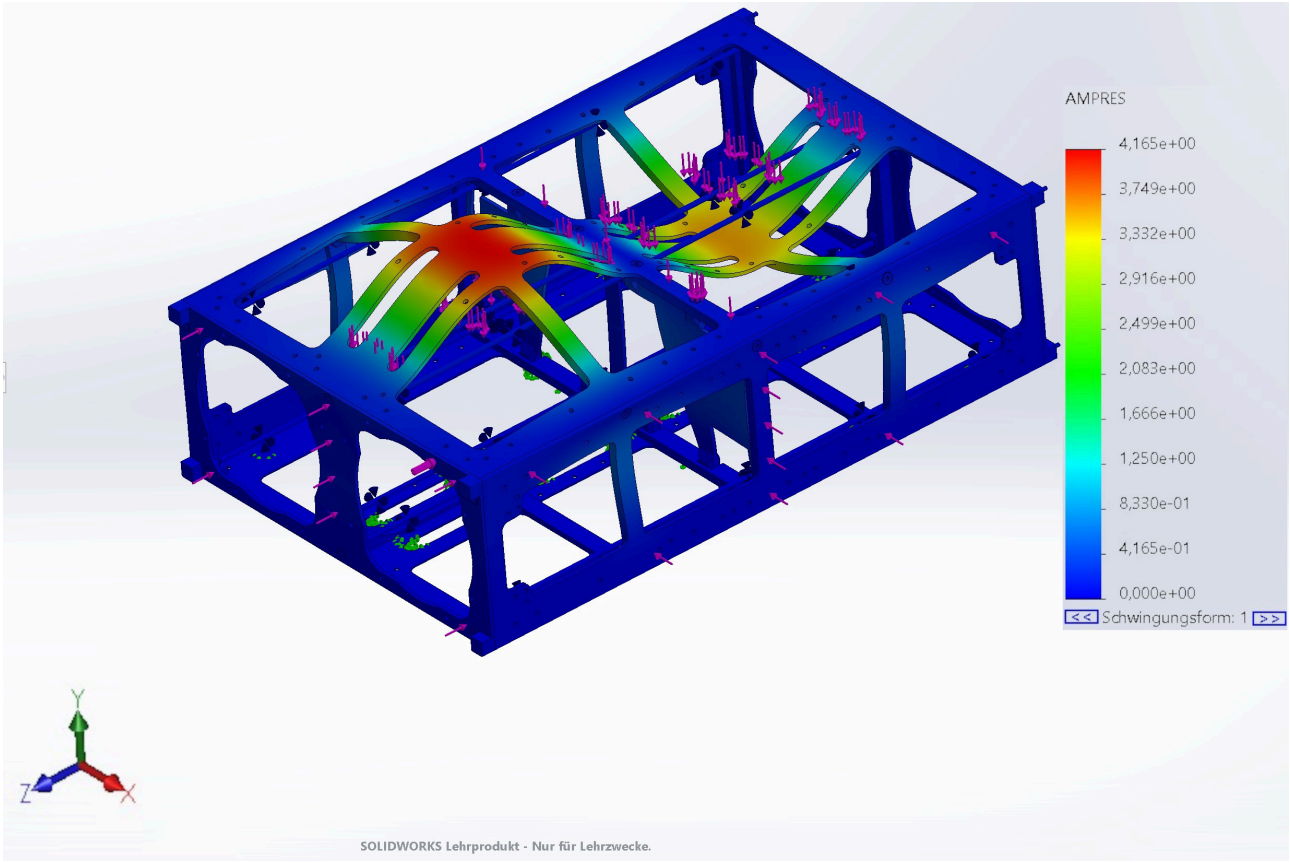

Figure 6.5 First mode of the EN-AW 6082 structure

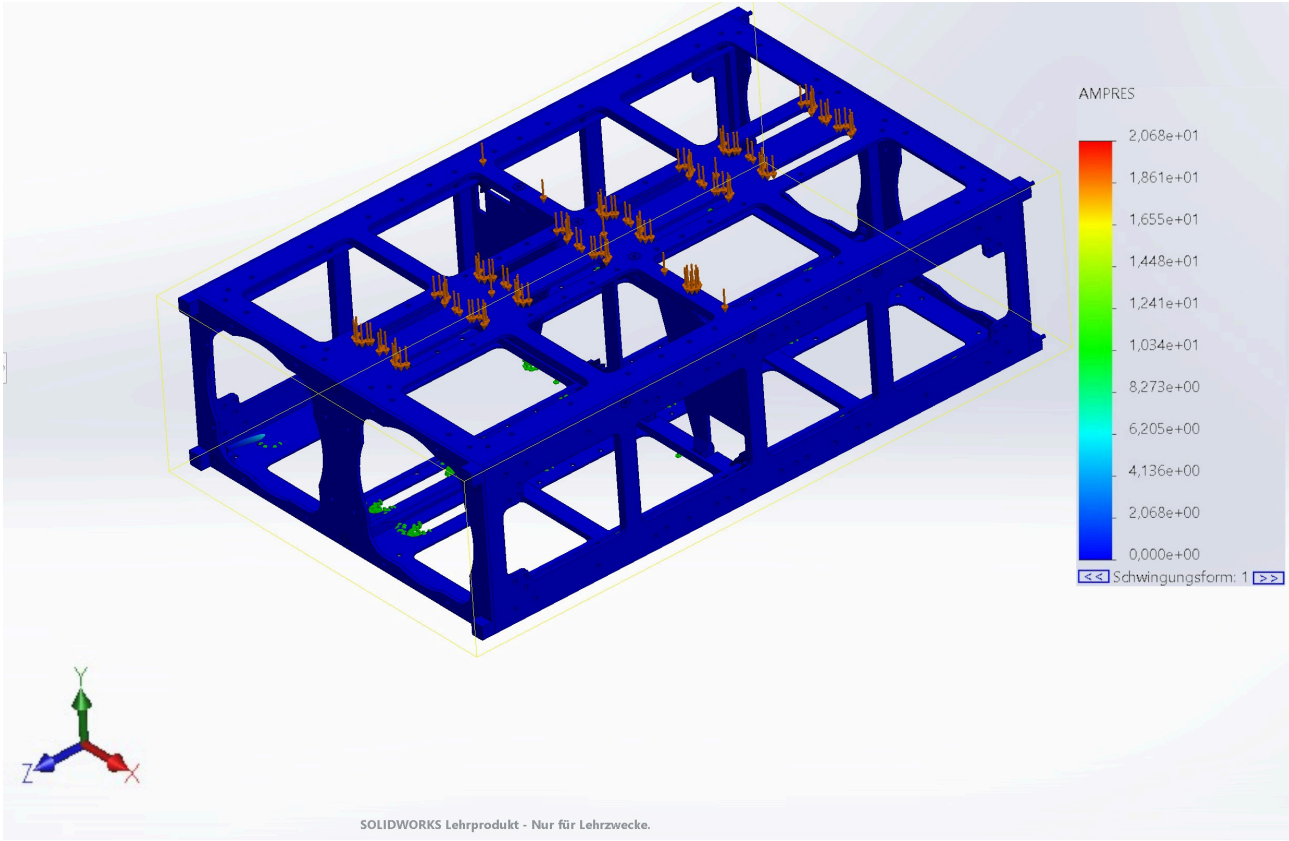

Figure 6.6 First mode of the WE43 structure

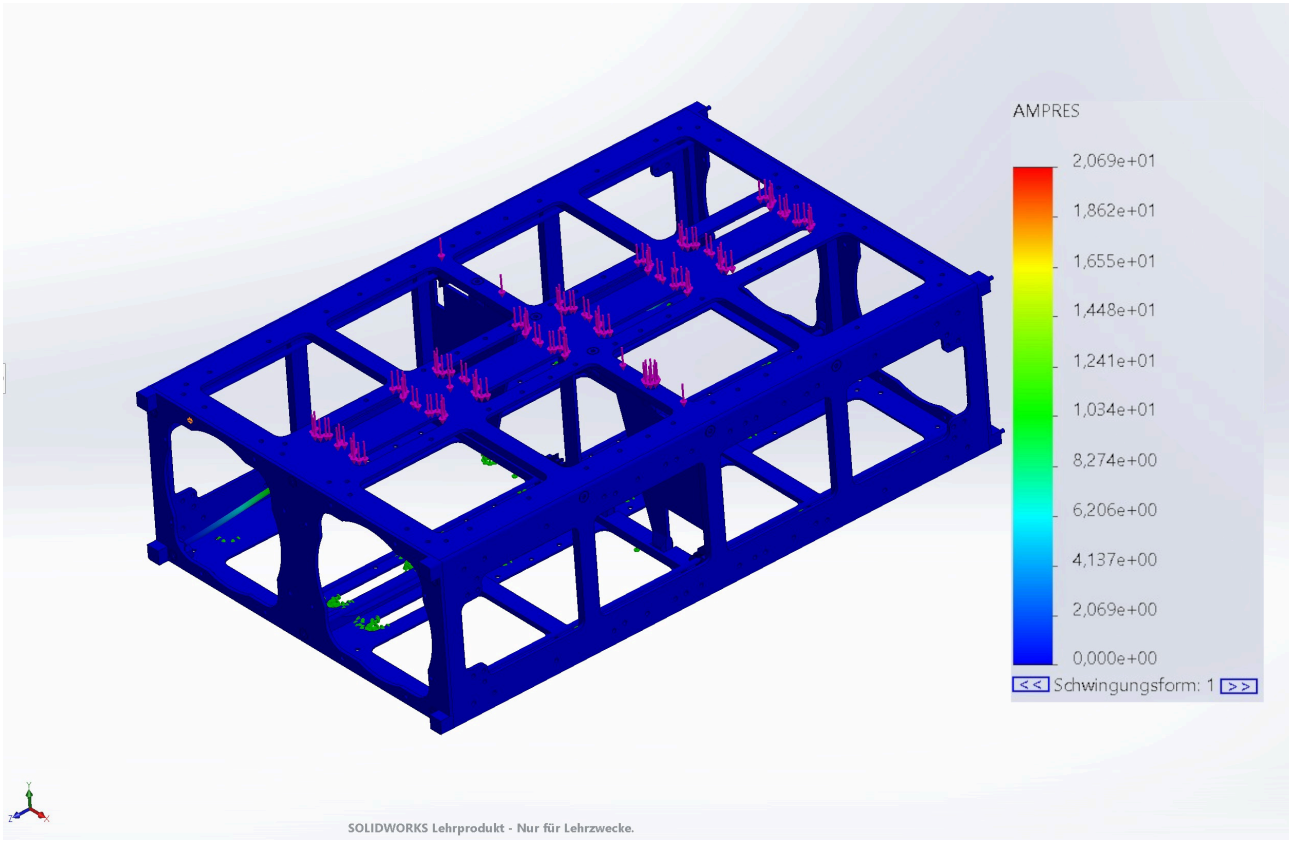

Figure 6.7 First mode of the WE43 lattice structure

6.3 Random Vibration Analysis

The random vibration analysis of the EN-AW 6082 structure displayed in Figure 6.8. The maximum calculated occurring Von-Mise stress is $6.385MPa$.
In Figure 6.9 the the resulting stress of the first mode of the structure due to excited random vibration. The first natural frequency is $f_0 = 291.54Hz$ and the resulting maximum von-Mise stress is $\sigma_{max} = 9.188MPa$. Both values are sufficient to meet the requirements.
The maximum stress due to random vibrations occurring on the structure displayed in Figure 6.10 $\sigma_{max} = 7.38MPa$. This is a neglectable load.

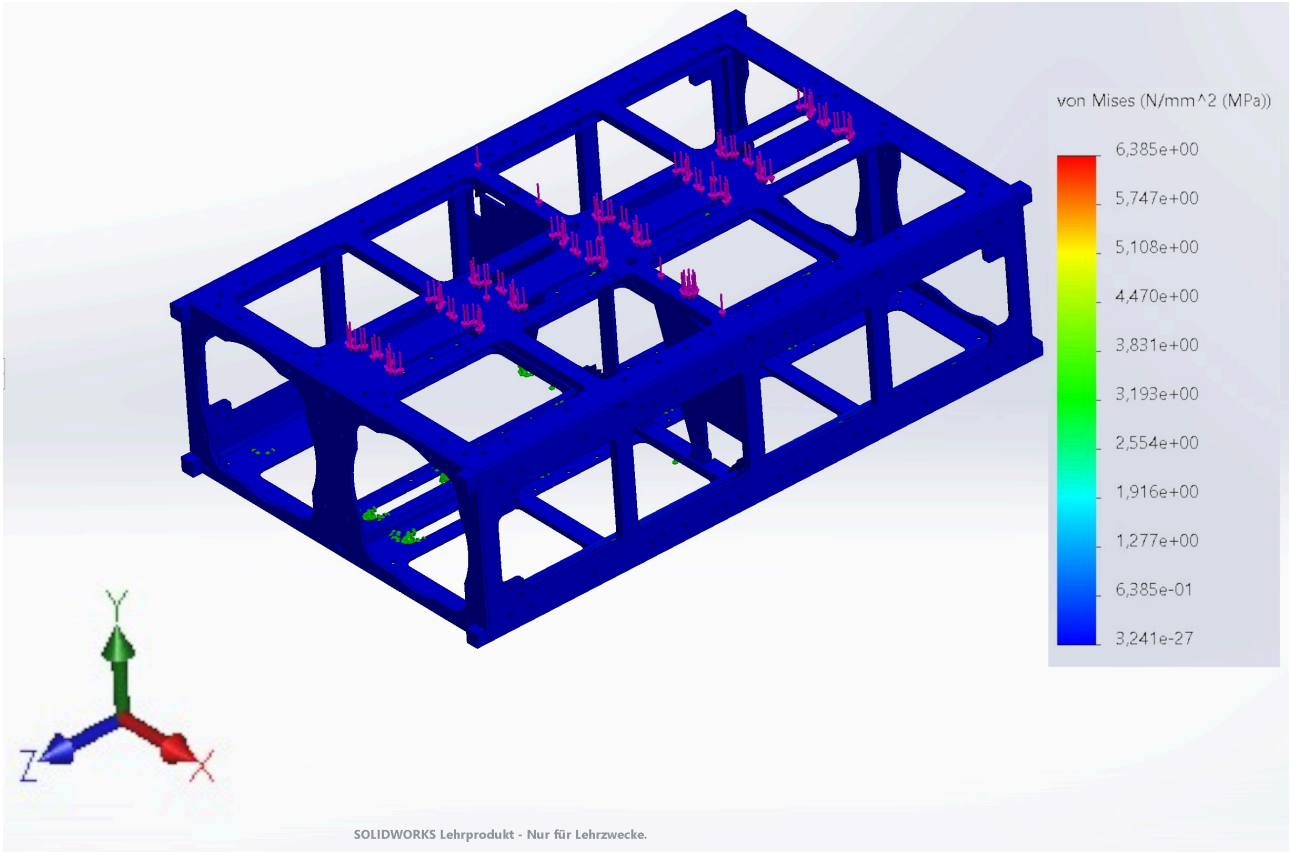

Figure 6.8 Resulting stress of the random vibration analysis with aluminum alloy

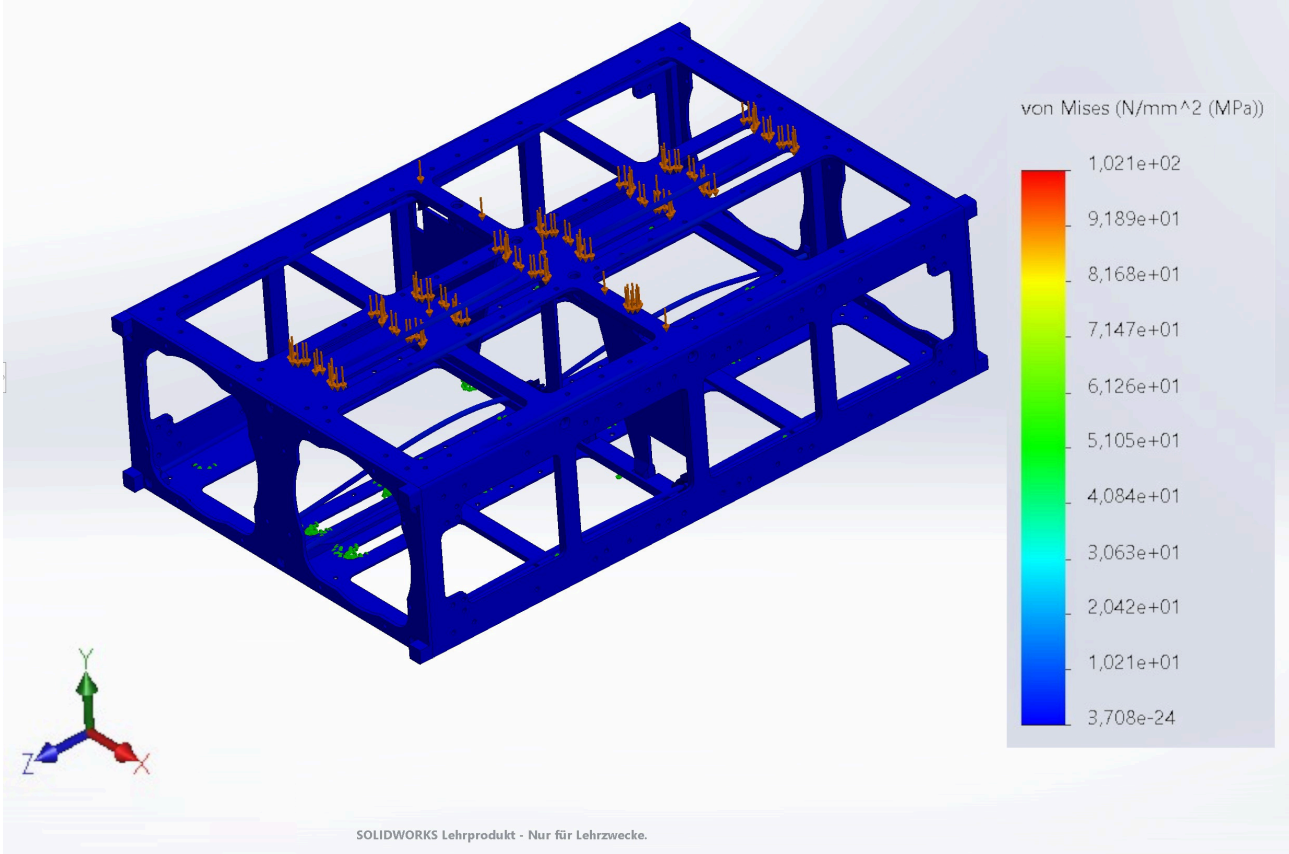

Figure 6.9 Von-Mise stress occurring at the structure made of WE43 due to random vibrations

6.4 Non-Linear Forces Analysis

Also it has to be accounted for non-linear forces. Figure 6.11 shows the typical longitudinal acceleration of a Ariane5 rocket. This graph was approximated as applied loads for the non-linear study. The maximum acceleration of $4.2g$ occurs after $100s$, in the manual it is mentioned that the acceleration does not exceed $4.55g$ and therefore this value was used as maximum acceleration instead. The applied loads result in Figure 6.11 in a maximum stress of $\sigma_{max} = 41.6MPa$ which is about 20% of the allowed stress.
The non-linear forces analysis of the WE43 structure shows in Figure 6.13 a resulting maximum occurring stress of $\sigma_{max} = 154MPa$.
The non-linear forces analysis of the WE43 micro lattice structure is the simulation that took the most time to calculate with 15.5 hours, the results displayed in Figure 6.13 shows a maximum occurring stress of $\sigma_{max} = 156MPa$

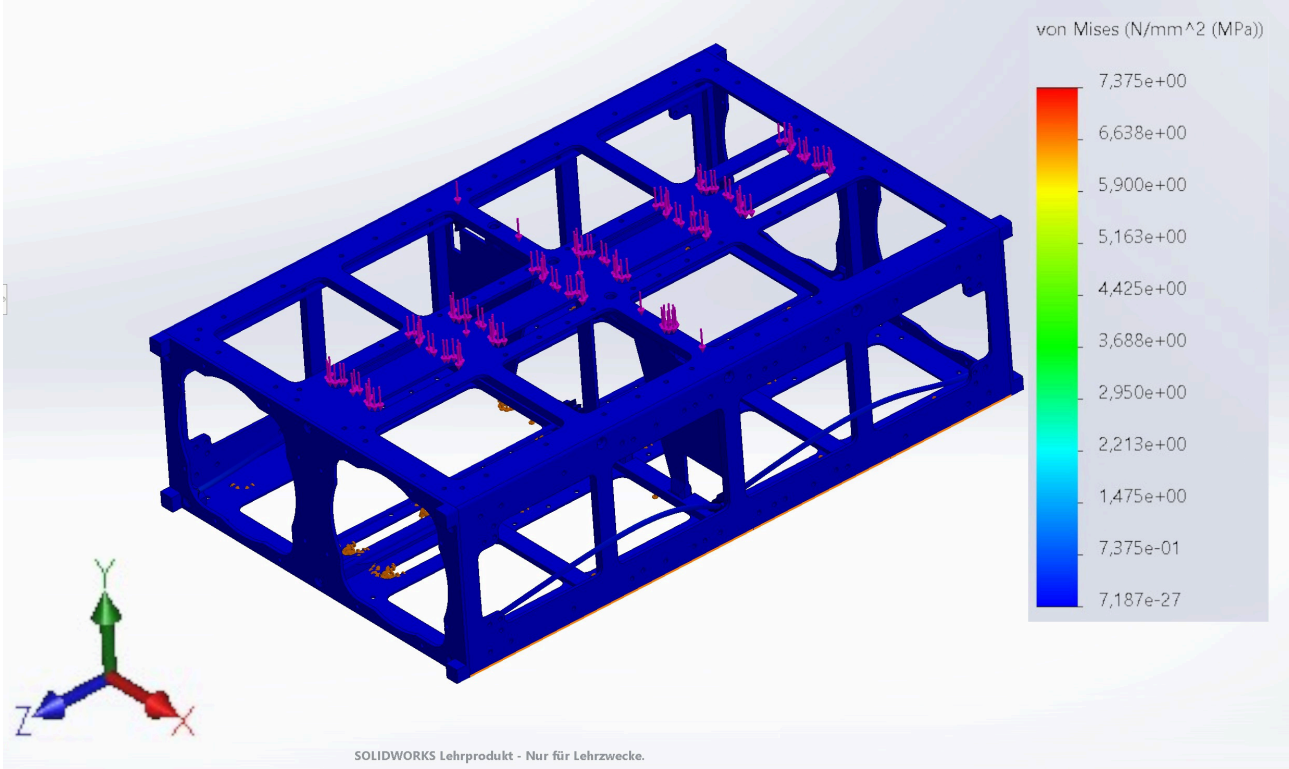

Figure 6.10 Stress results of the random vibration analysis of the WE43 micro lattice structure

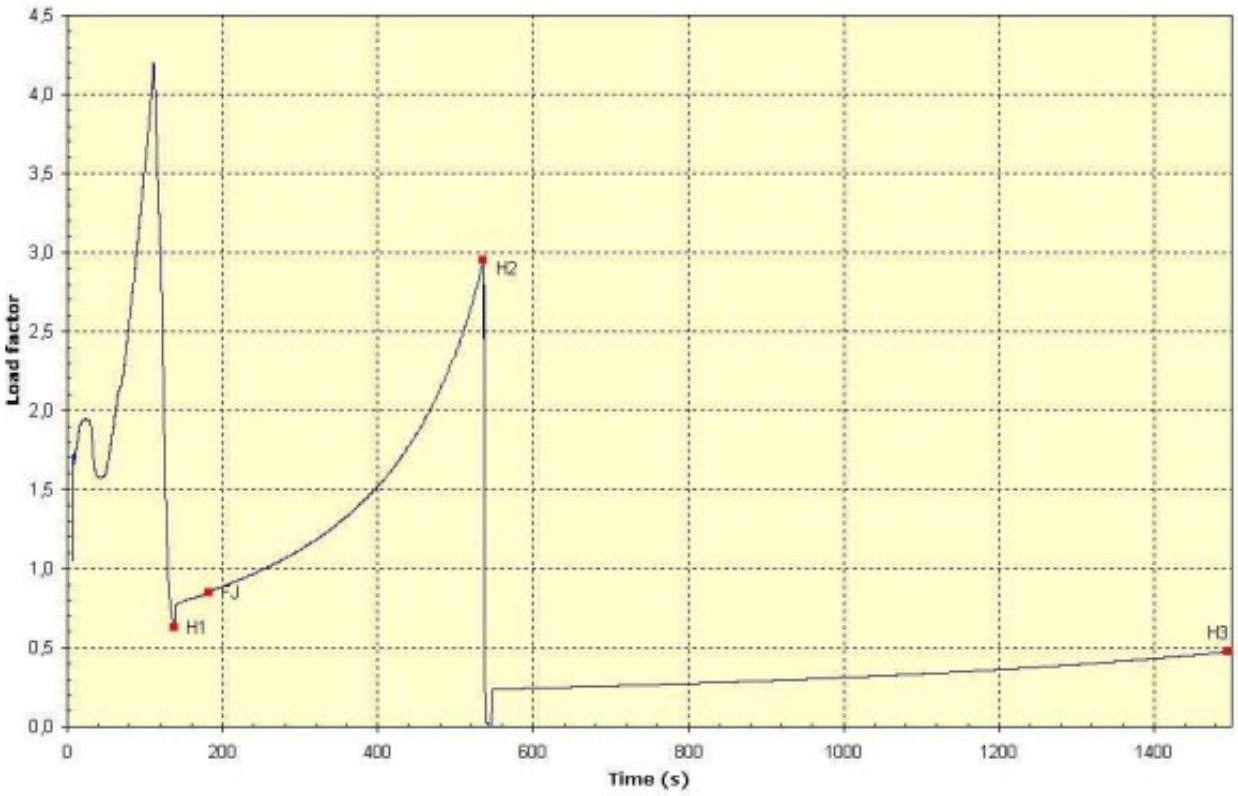

Figure 6.11 Ariane5 typical longitudinal acceleration[23]

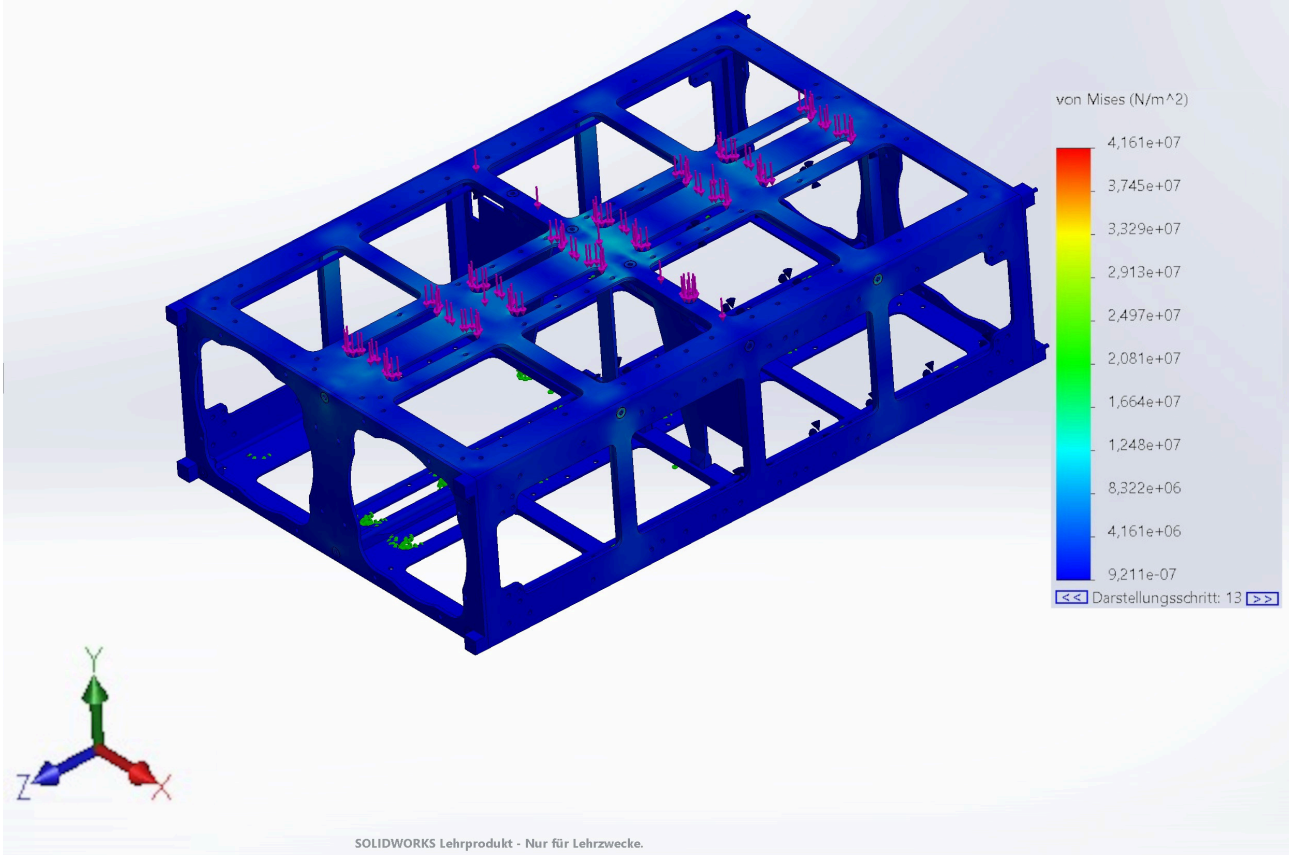

Figure 6.12 Stress results of the non-linear analysis with the applied loads of the Ariane5 rocket

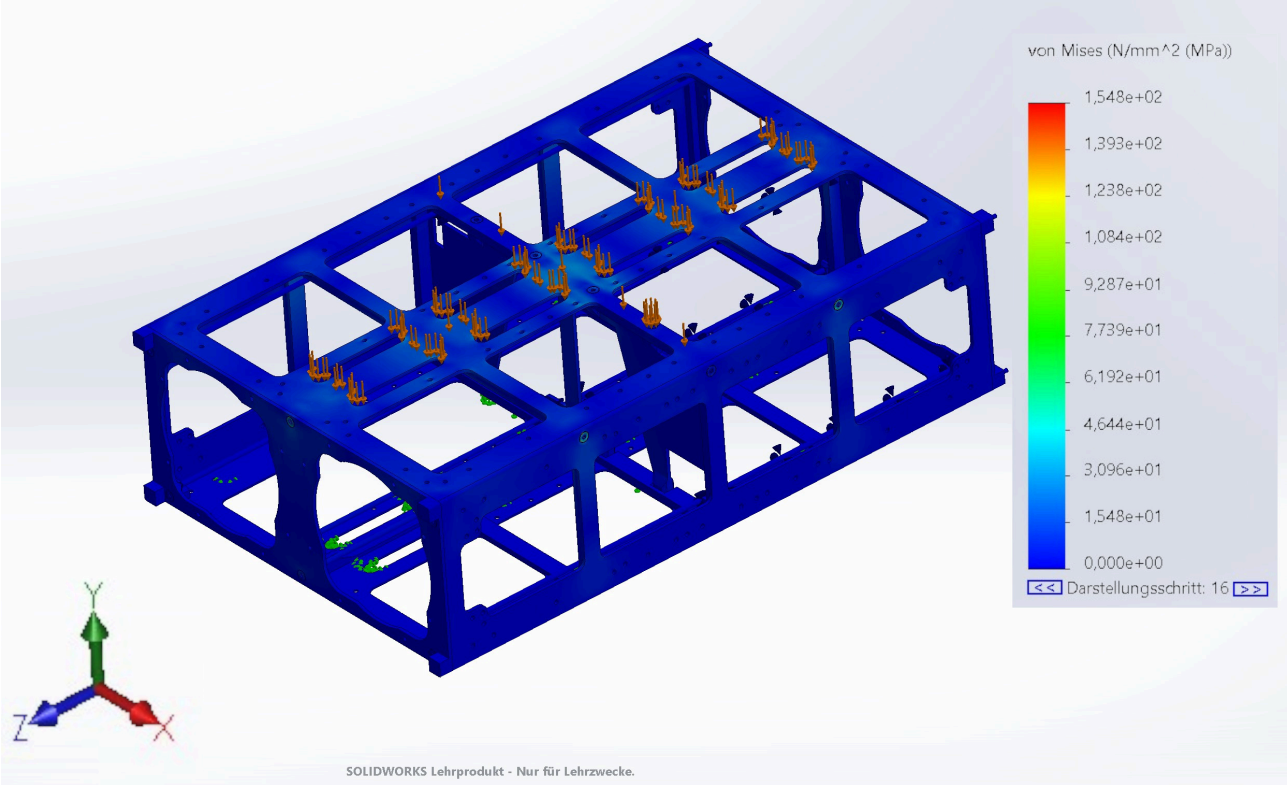

Figure 6.13 Mechanical stress results of the non-linear forces analysis of the 6U CubeSat structure made out of the WE43

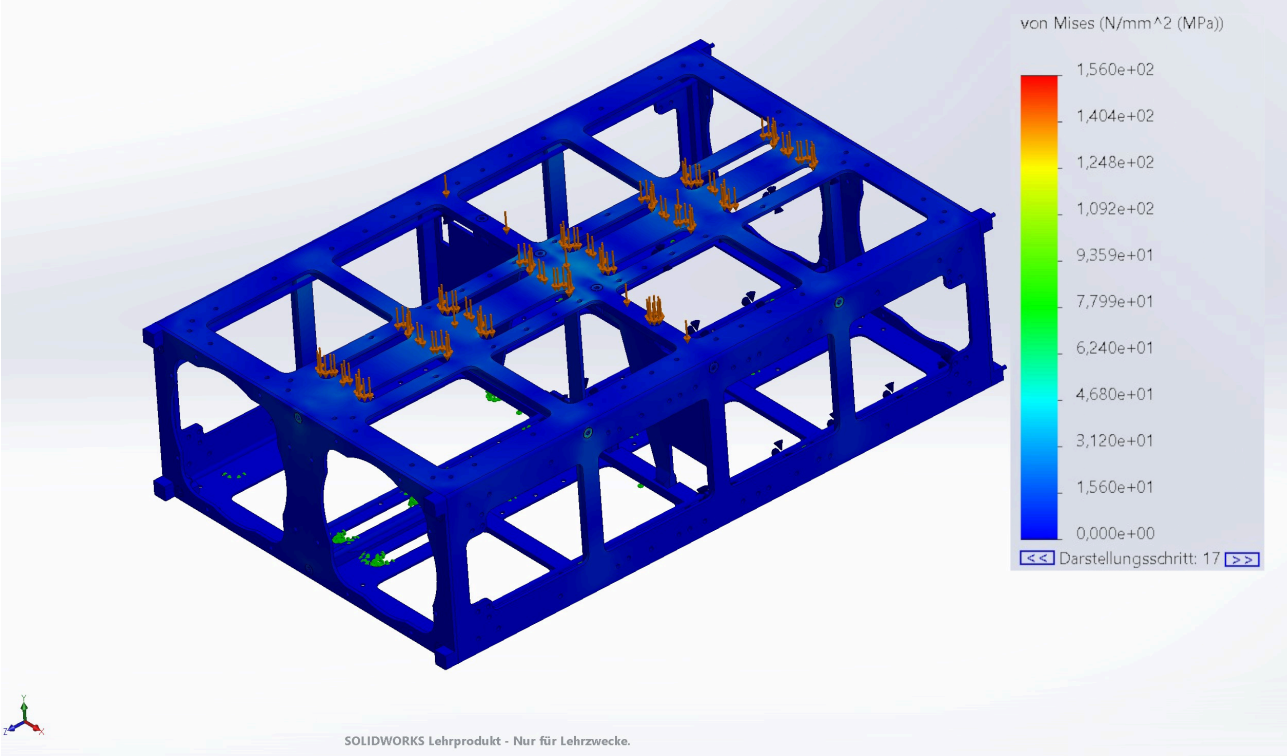

Figure 6.14 Stress results of the non-linear forces simulation of the WE43 micro lattice structure

All relevant results are again displayed in Table 6.1. It is clearly visible, that the Aluminum is the best resistant material to mechanical loads out of those three materials. But the EN-AW 6082 structure, the WE43 structure fulfill the requirements and therefore could proceed to production and testing. The WE43 lattice structure needs to be supplemented by WE43 at the bottom corners to withstand the maximum occurring stresses with a factor of safety of 2.

	Unit	EN-AW 6082	WE43	WE43 micro lattice
One axis static analysis				
Maximum stress	MPa	130	292.9	298
Maximum strain	Equivalent Strain	1.2E-3	4.302E-3	4.35E-3
Maximum displacement	mm	0.297	0.869	0.507
Frequency analysis				
First natural frequency	Hz	293.8	291.7	291.5
Random vibration analysis				
Maximum stress	MPa	6.385	9.188	7.375
Non-linear forces analysis				
Maximum stress	MPa	41.6	154.8	156
Maximum strain	Equivalent Strain	2.1E-4	3.3E-4	8.2E-4
Maximum displacement	mm	0.106	0.18	0.45

Table 6.1 Mechanical simulation results of the EN-AW 6082, WE43 and WE43 micro lattice structures in comparison

7 Re-entry Simulation

Figure 7.1 is a picture of the 6U CubeSat model in the SARA tool of DRAMA. The solar panel on the top and the structure beneath it are visible. All parts are just basic geometry simplifications. SARA uses a parent-child relationship modelling approach. Hence the satellite demises in this simulation in the way, that only after the parent object experienced total demise, the child objects start the demise. For this model, there are some basic CubeSat components put inside to get a appropriate test mass and also to study the different demise behaviours. The most critical parts are the components made out of materials with very high melting points like the reaction wheels that have a titanium case and are in this simulation made of solid TiAl6V4.
The settings used for the simulation were the standard settings for the Keplerian elements with an uncontrolled re-entry.

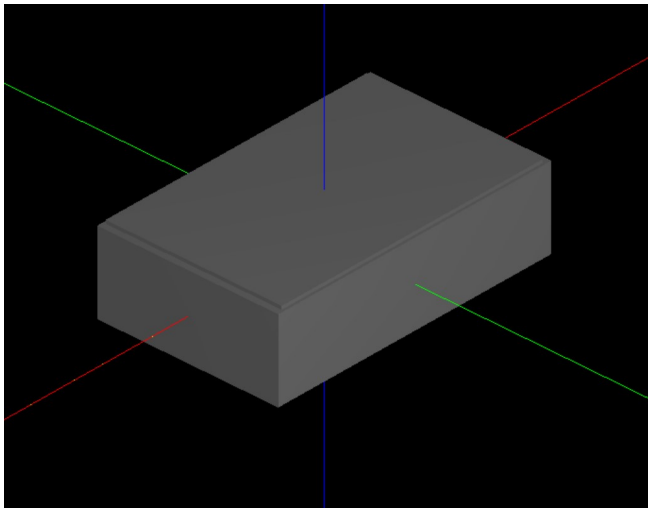

Figure 7.1 6U CubeSat model in SARA

Figure 7.2 shows the simulation results for the re-entry simulation of a 6U CubeSat with the structure made out of EN-AW 7075. The alloy En-AW 7075 is chosen, because the demise behaviour of this alloy is tested in the wire-arc wind tunnel of the German Aerospace Center (DLR) and the demise behaviour is to be expected about the same as EN-AW 6082. The altitude is hereby plotted over the time. The different colors of the flight path show what the current configuration of the satellite is and in which stage of demise it is. The blue crosses are marking the points where a component is fully demised. The first two components that are fully demised are the solar panel followed by the structure at an altitude of $94.25km$. The last component to be demised is the reaction wheel at an altitude of $18km$. This simulation shows that for a 6U CubeSat there would be no need of acting, since it fully demises with an aluminum alloy structure.

Figure 7.3 shows the simulation results for the satellite with a magnesium alloy structure. Notable and very interesting is that even though all simulation parameters except the material of the structure remain the same, the flight path of the satellite changes. It ascends from the entry interface a little bit before descending. This results in a longer time to demise if started counting at the moment, when the satellite reaches the entry interface the first time. If counting is started for example when the satellite crosses the 120km altitude border, the time is almost similar. The structure is in this case fully demised at an altitude of $96km$.

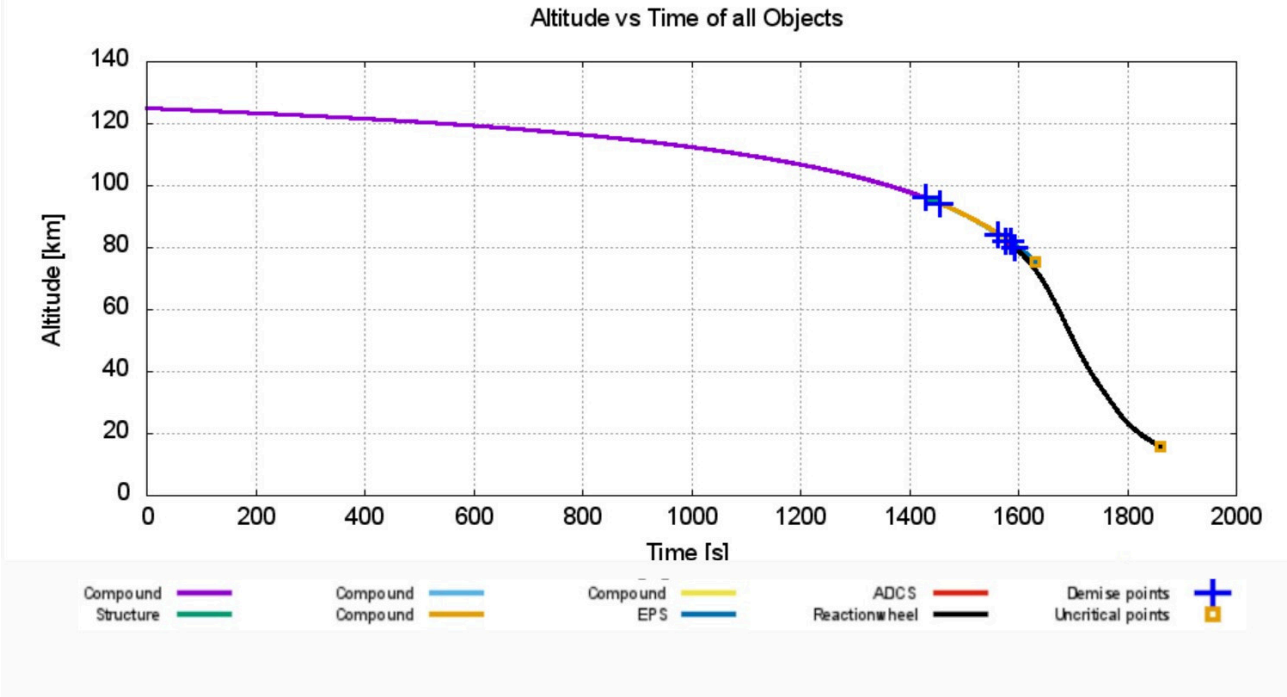

Figure 7.2 Altitude over time graph of the re-entry simulation of the 6U CubeSat with the structure made out of EN-AW 7075

Figure 7.3 Altitude over time graph of the re-entry simulation of the 6U CubeSat with the structure made out of WE43

Figure 7.4 shows the simulation results for the satellite with a magnesium alloy lattice structure. Compared with the flight path of solid magnesium alloy structure, this one does not show the slight ascend, after reaching entry interface. Nevertheless the demise happens in an overall similar time frame. The structure is in this case fully demised at an altitude of $96.7km$.
concluding that the magnesium structure demises faster, with a difference of $2.7km$ in altitude and the lattice structure adds another $700m$ to this. The earlier demise of the structure also results in an earlier demise of the components inside, but in the case of this CubeSat the casualty risk is 0 for all structures, so for 6U CubeSats the material selection does not matter in this regard.

In Figure 7.5 for each of the materials investigated above the effect of the wall thickness on the demisability is simulated. There is a clearly visible drop of demisability at a wall thickness of 8mm and it is not clear where this behaviour originates from. The benefit that can be obtained from the material choice scales with the material thickness, the benefit factor b defined in (7.1) with h_0 being the altitude of demise of the aluminum alloys structure and h_1 being the altitude of the structure that is compared. The benefit factor for WE43 is $b = 1.0186$ at a wall thickness of 1mm and $b = 1.0871$ at a wall thickness of 1cm. For the micro lattice structure at a thickness of 1mm $b = 1.0262$ and at a thickness of 1cm $b = 1.133$. Therefore the benefit gain for the micro lattice is almost double the benefit gain of the solid WE43.

$$b = \frac{h_1}{h_0} \tag{7.1}$$

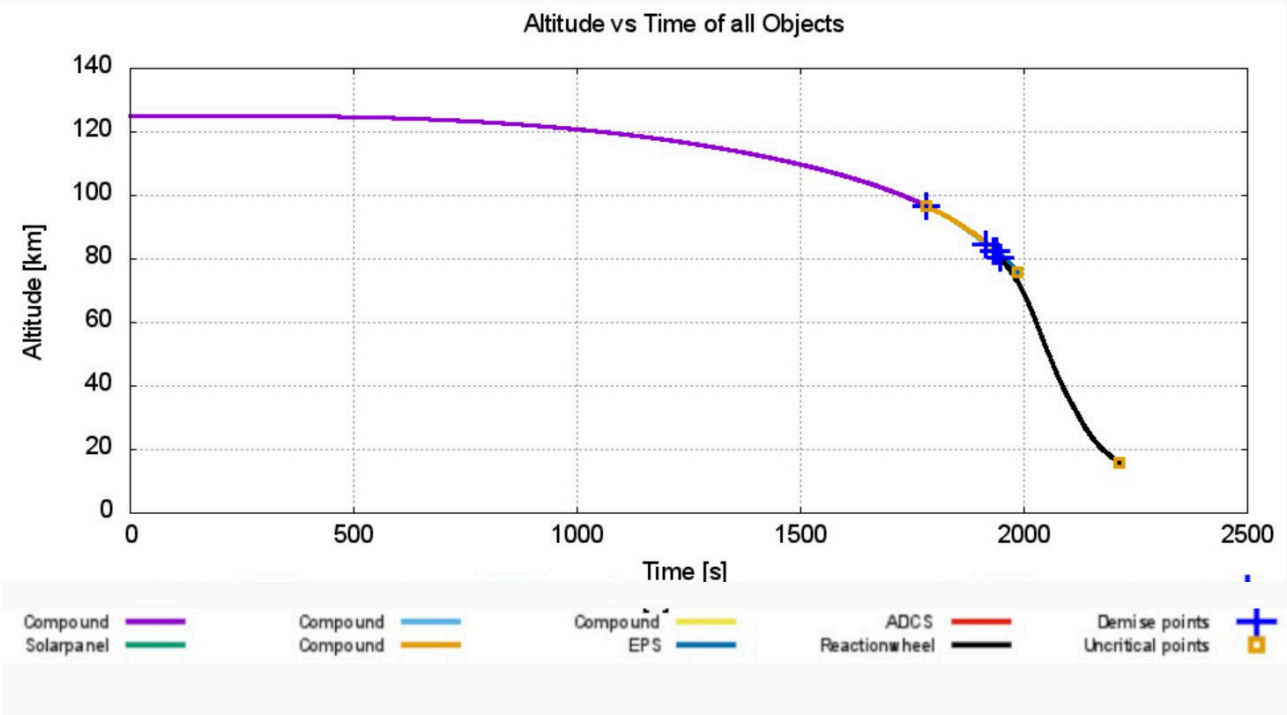

Figure 7.4 Altitude over time graph of the re-entry simulation of the 6U CubeSat with the structure made out of WE43 micro lattice

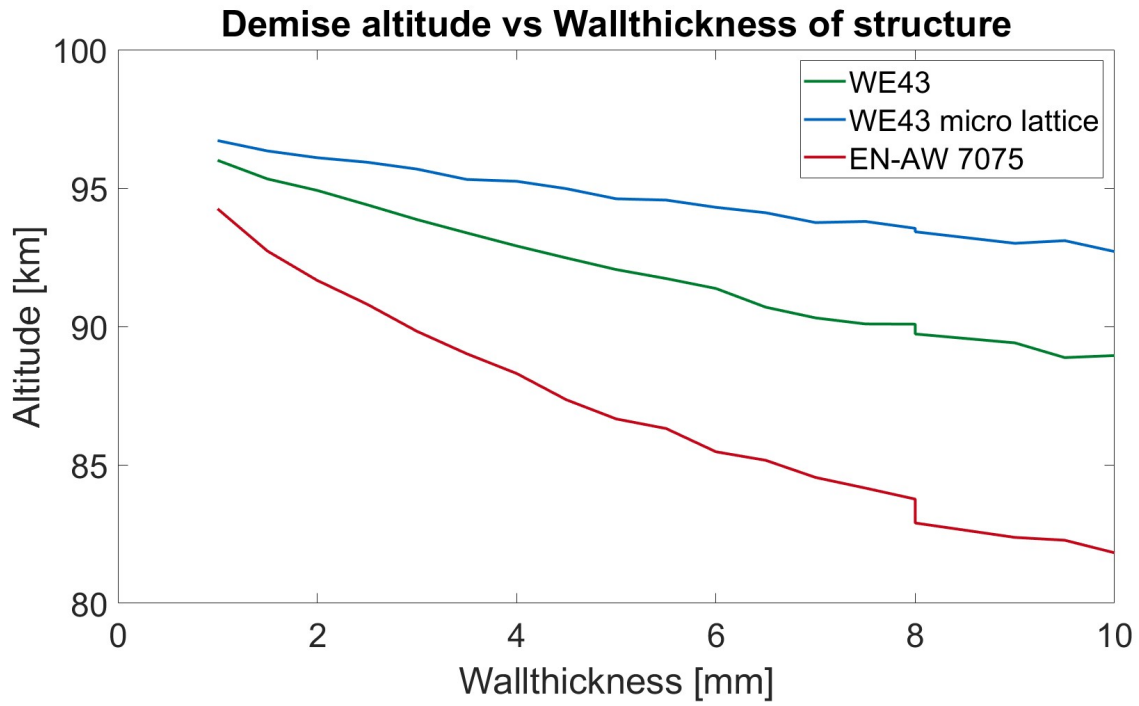

Figure 7.5 Altitude of demise in dependence of thickness of the wall of the structure

8 Scaling

Scaling of the results for larger spacecrafts may become difficult in reality. The manufacturing capabilities for large additive manufactured magnesium alloy parts are not yet there, except for wire arc additive manufacturing methods, but this method comes with a limited possible level of detail. This results in a larger minimal strut diameter of the lattice unit cells, what then results in a bigger unit cell and therefore weaker mechanical properties, what then results in a higher volume cost for the same structural integrity.
Since volume and mass both are very valuable parameter in spaceflight due to the limited capacity of launch vehicles this is a huge drawback for this manufacturing method.
On the other side the results for solid magnesium alloys can be scaled very well, since these parts can be additive manufactured in larger dimensions. But probably the manufacturing capabilities for larger magnesium alloy parts with techniques like powder bed fusion will be expanded in the future and this should not be a problem then.

For the investigation of the scaling of the results regarding re-entry the standard model of a satellite from DRAMA was used, because of a lack of detailed information over existing missions and just for simplification reasons. The structure model is shown in Figure A.7. For this structure with the material EN-AW 7075 applied for both containments, the results are shown in Figure 8.1. The first structure called SVM demises at an altitude of $h_{1al} = 79.919km$ and the second containment called PLM demises at an altitude $h_{2al} = 69.956km$.
In Figure 8.2 the results of the simulation with WE43 are shown and alone from the number of legend entries it hints that this structure is better demisable, since there is a new legend entry created for each free flying object, which originate at breakups of their parent structure.
The SVM demises at an altitude of $h_{1mg} = 87.439km$ and the PLM this time demises at an altitude of $h_{2mg} = 82.361km$. This already shows the effect the material change can have. If we now look at the micro lattice structure in Figure 8.3, the altitude of demise of the SVM $h_{1ml} = 91.243km$ and the altitude of demise of PLM is $h_{2ml} = 88.777km$. So this shows that the results from the CubeSat are scalable up to bigger sizes of satellites. The graphs also show a severe reduction of the number of fragments impacting. This results in a smaller risk of casualties on ground. The risks are listed in Table 8.1.

Structure material	Total casualty area $[m^2]$	Total impact mass $[kg]$	Total casualty probability	Total number of fragments
EN-AW 7075	63.85	874.86	7.431E-4	46
WE43	35.12	543.70	4.243E-4	19
WE43 micro lattice	33.09	478.8	2.369E-4	18

Table 8.1 Risk assessment of the different structures

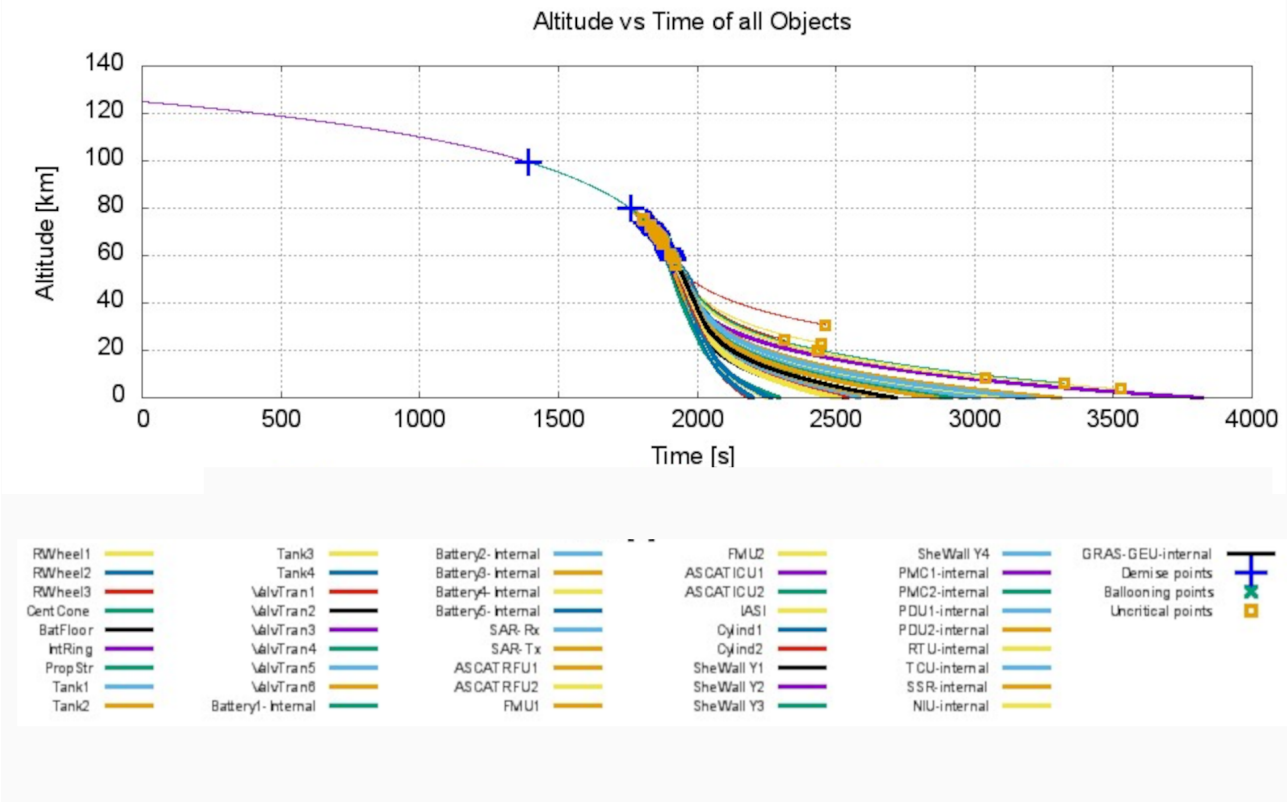

Figure 8.1 Altitude over time graph for all fragments of the satellite with a structure made out of the aluminum alloy EN-AW 7075

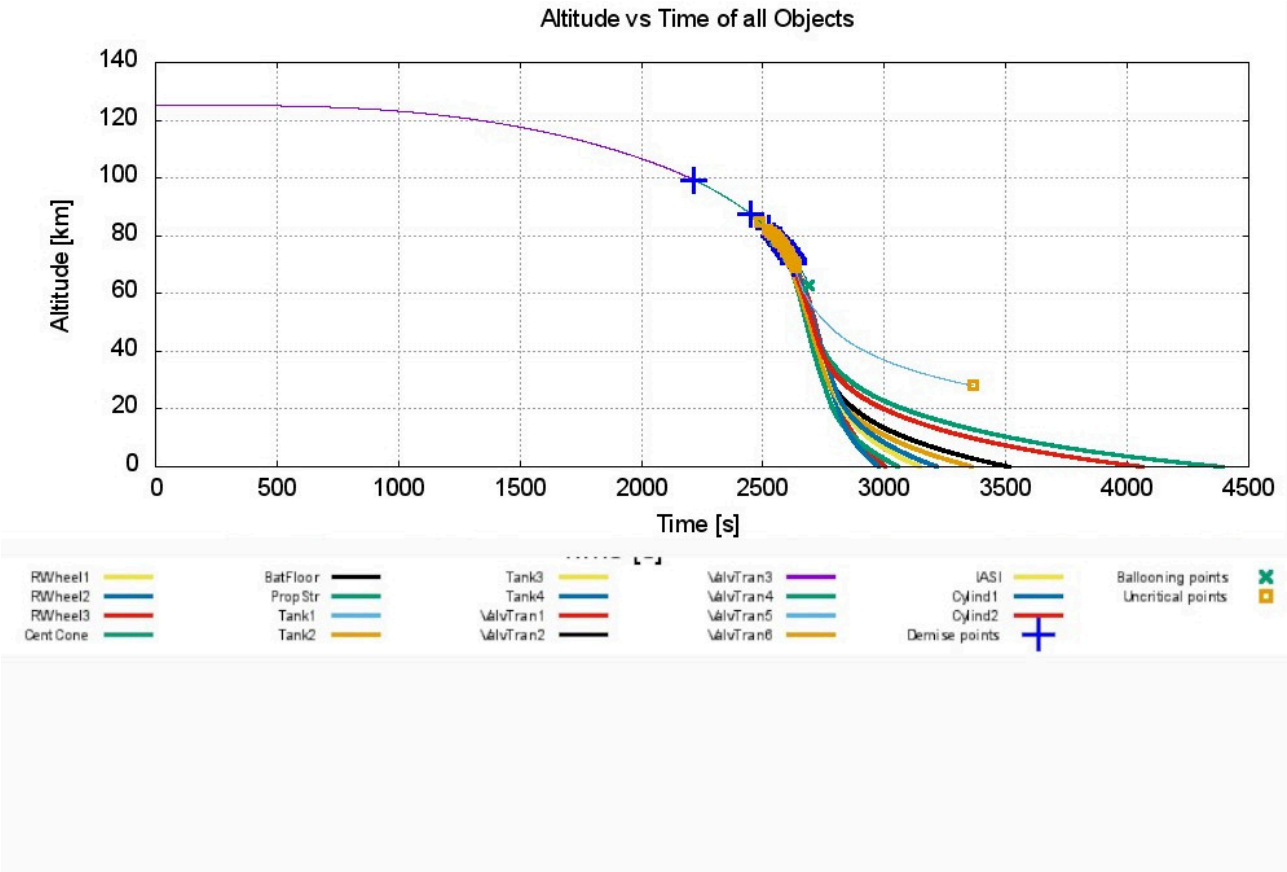

Figure 8.2 Altitude over time graph for all fragments of the satellite with a structure made out of WE43

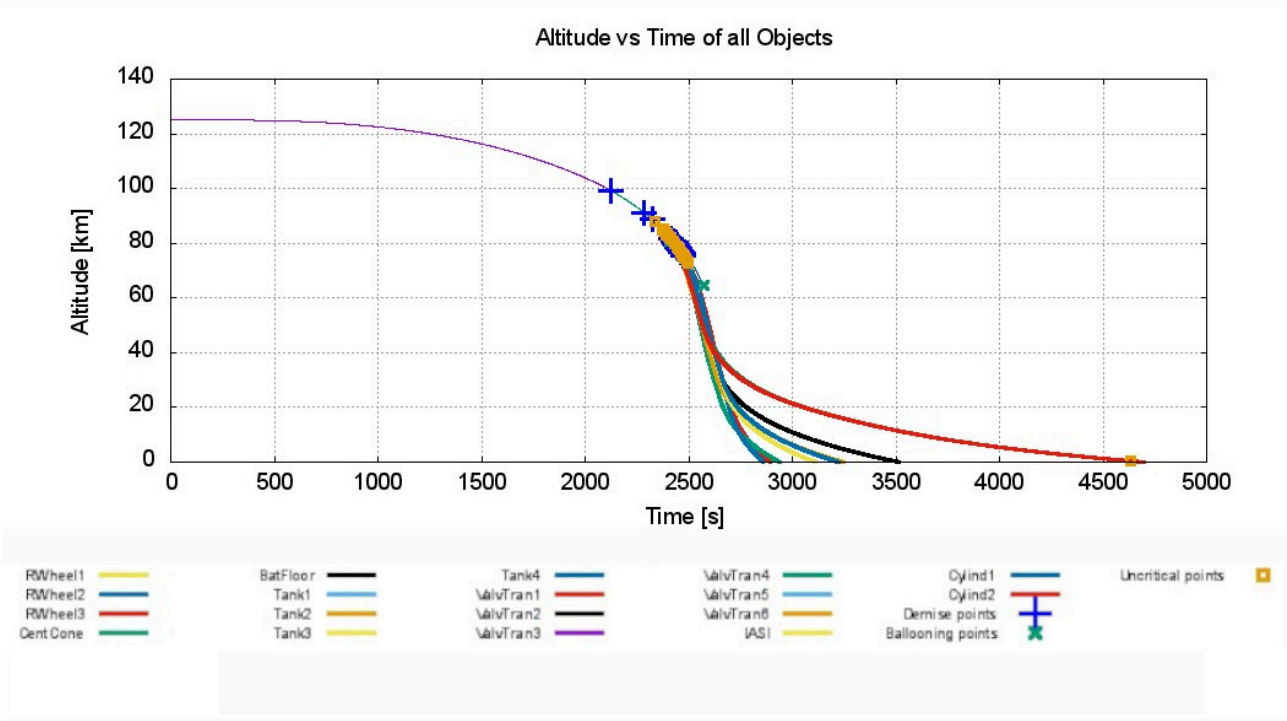

Figure 8.3 Altitude over time graph for all fragments of the satellite with a structure made out of WE43 micro lattice

9 Conclusion and Possible Next Steps

9.1 Conclusion

The capabilities of magnesium alloys especially WE43, in solid and micro lattice form, regarding the structural integrity of a CubeSat structure and the influence of satellite demise compared to aluminum alloys were researched. It was found that magnesium alloys have an improved demisability behaviour compared to aluminum alloys. The more material used the larger was the difference in the demise altitude.

9.2 Possible Next Steps

The structure will be manufactured with Aluminum EN-AW 6082 and will undergo a testing and verification process. It would also be possible to manufacture the structure with WE43 and if a suitable additive manufacturing tool with a sufficient resolution is available also the micro lattice structure could be manufactured and tested. The results of this process can verification the simulation results presented in this document. Furthermore magnesium alloys should be tested in a wire arc wind tunnel or similar to better understand the demise behaviour. In addition a experimental series to determine values required for SARA, like the Catalytic recombination coefficient for oxygen and nitrogen dissociation reactions, the reaction probability for magnesium oxide and atomic oxygen and the emission coefficient for the complete temperature profile up tho the melting point could be set up.

A Appendix

The Solidworks simualtion results are shown here.

Static load analysis:

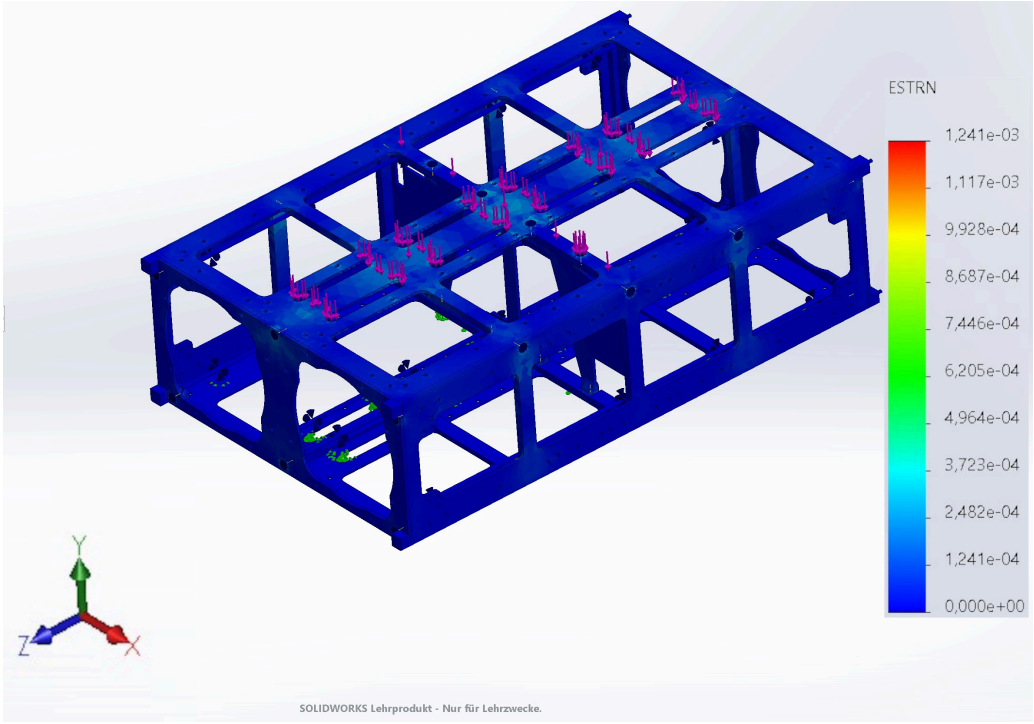

Figure A.1 Mechanical strain results of the static load analysis of the 6U CubeSat structure made out of EN-AW 6082 with a force of 1200N applied in negative Y-direction

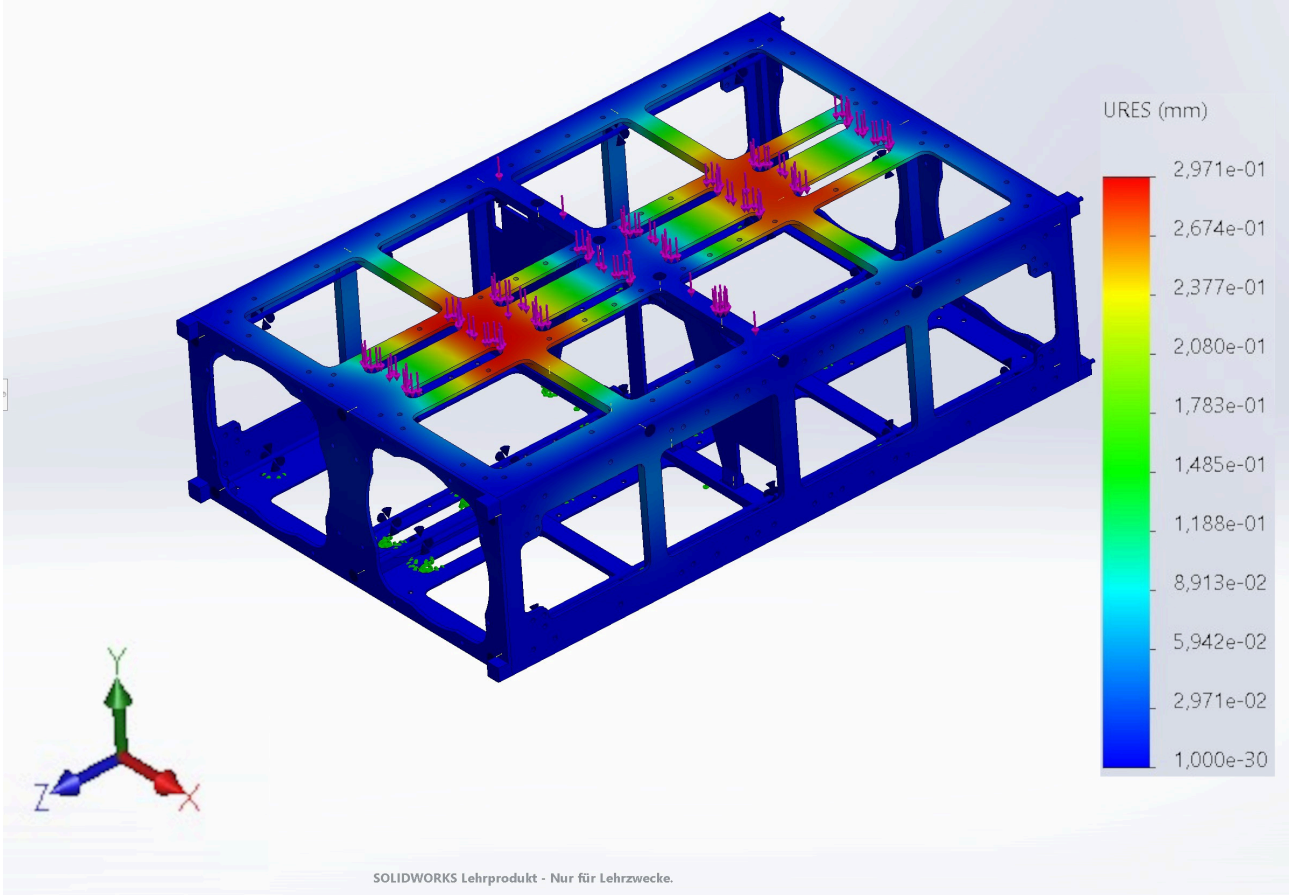

Figure A.2 Displacement results of the static load analysis of the 6U CubeSat structure made out of EN-AW 6082 with a force of 1200N applied in negative Y-direction

The structure of the standard satellite is shown in Figure A.7. This structure was used to assess the scalability of the proposes of this thesis. The only changes to this structure were the change of materials of the two outer structures PLM and SVM.

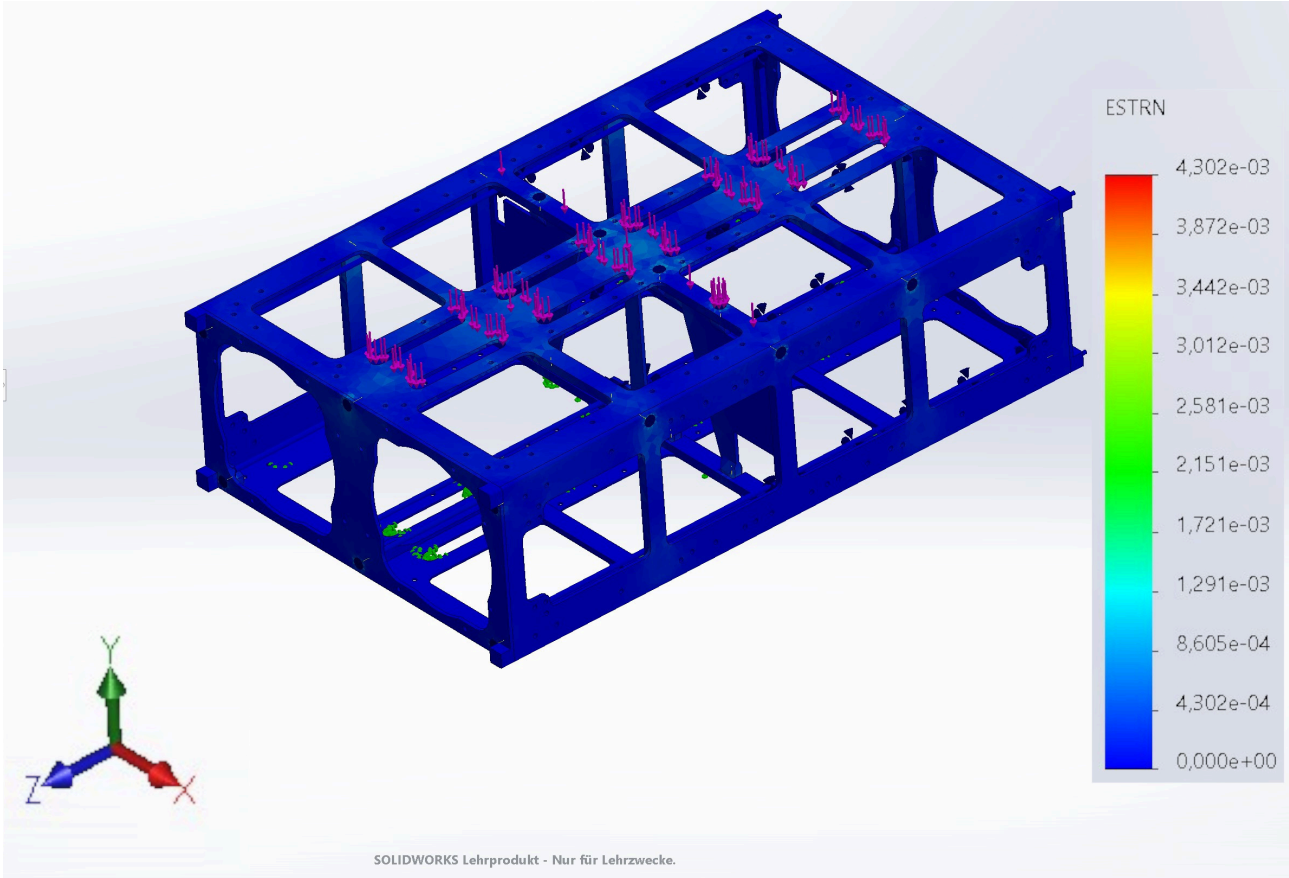

Figure A.3 Mechanical strain results of the static load analysis of the 6U CubeSat structure made out of WE43 with a force of 1200N applied in negative Y-direction

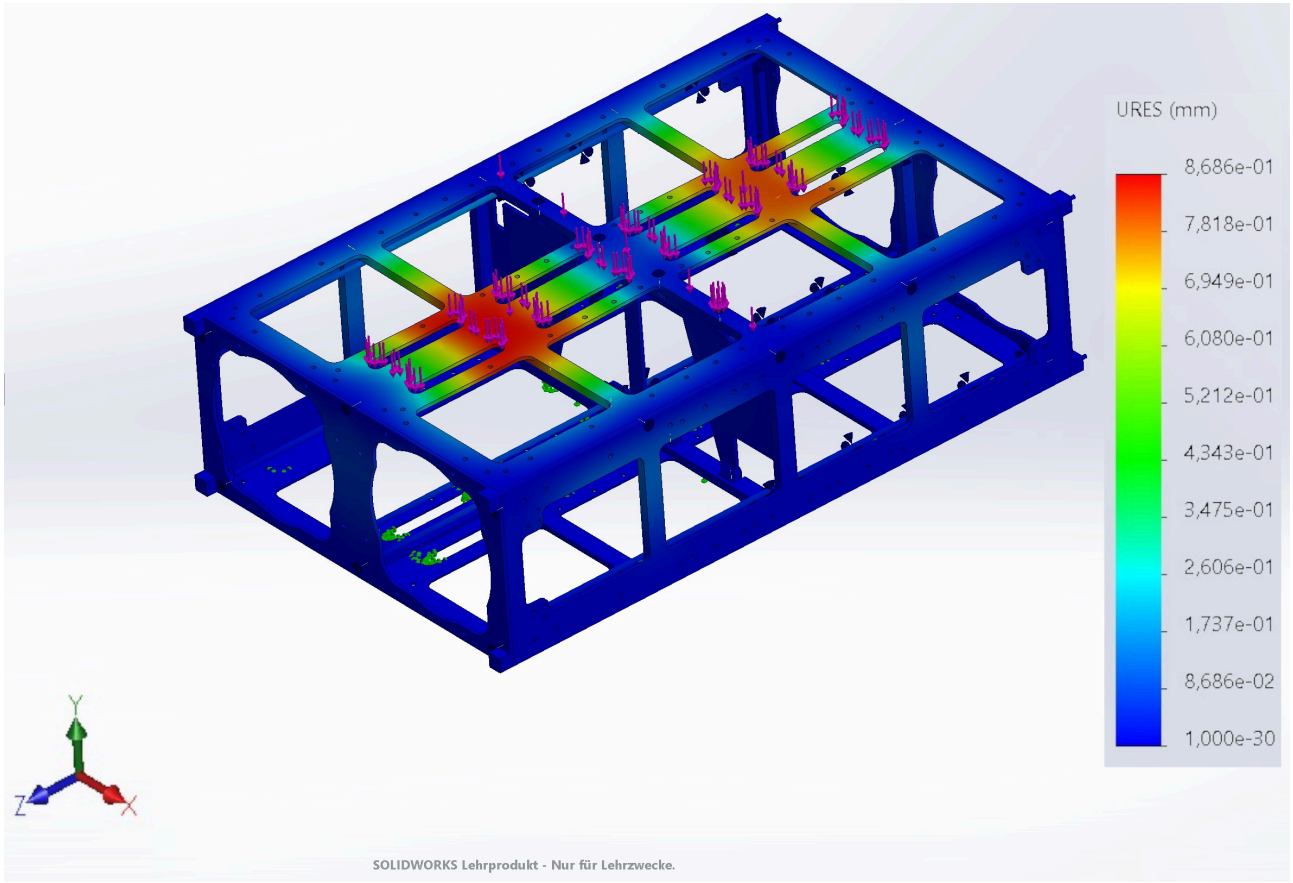

Figure A.4 Displacement results of the static load analysis of the 6U CubeSat structure made out of WE43 with a force of 1200N applied in negative Y-direction

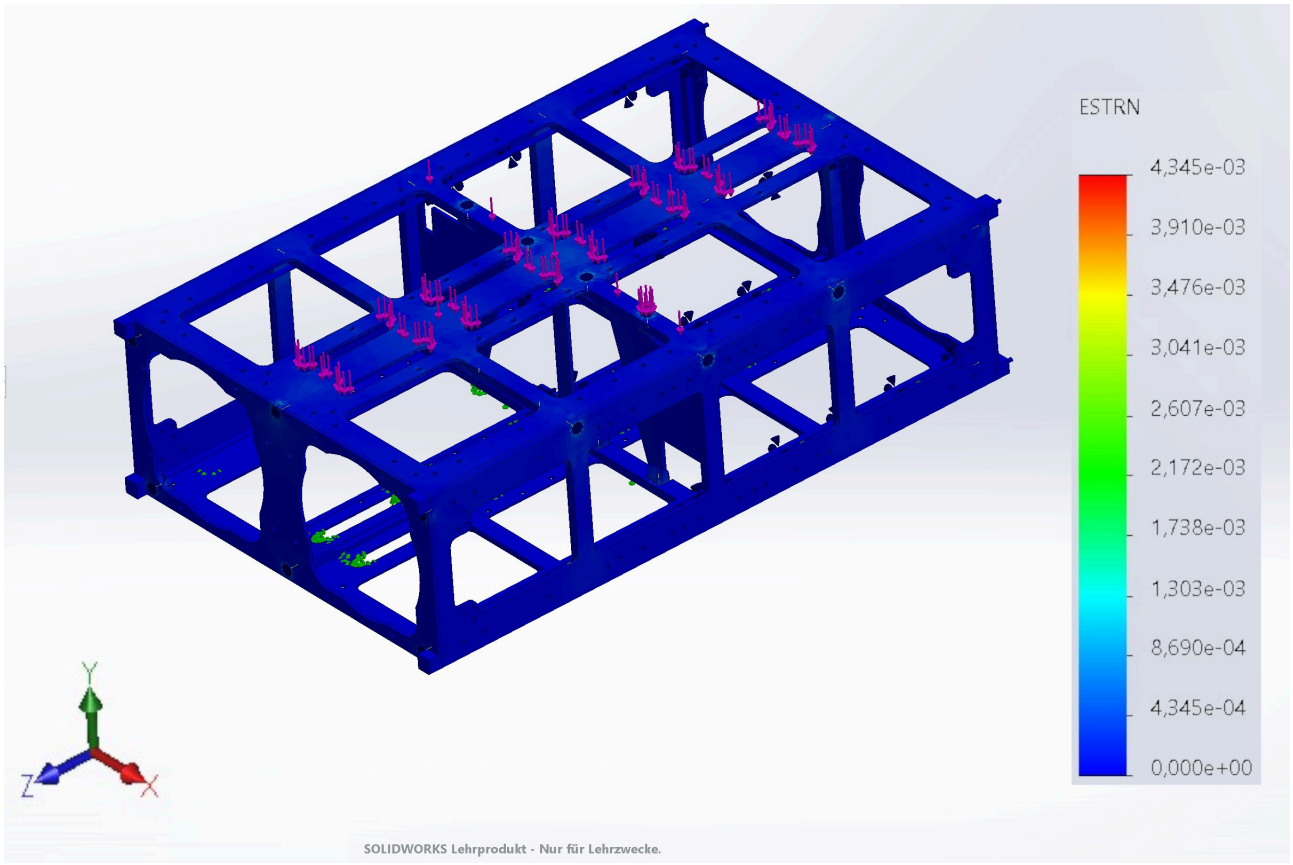

Figure A.5 Mechanical strain results of the static load analysis of the 6U CubeSat structure made out of WE43 micro lattice with a force of 1200N applied in negative Y-direction

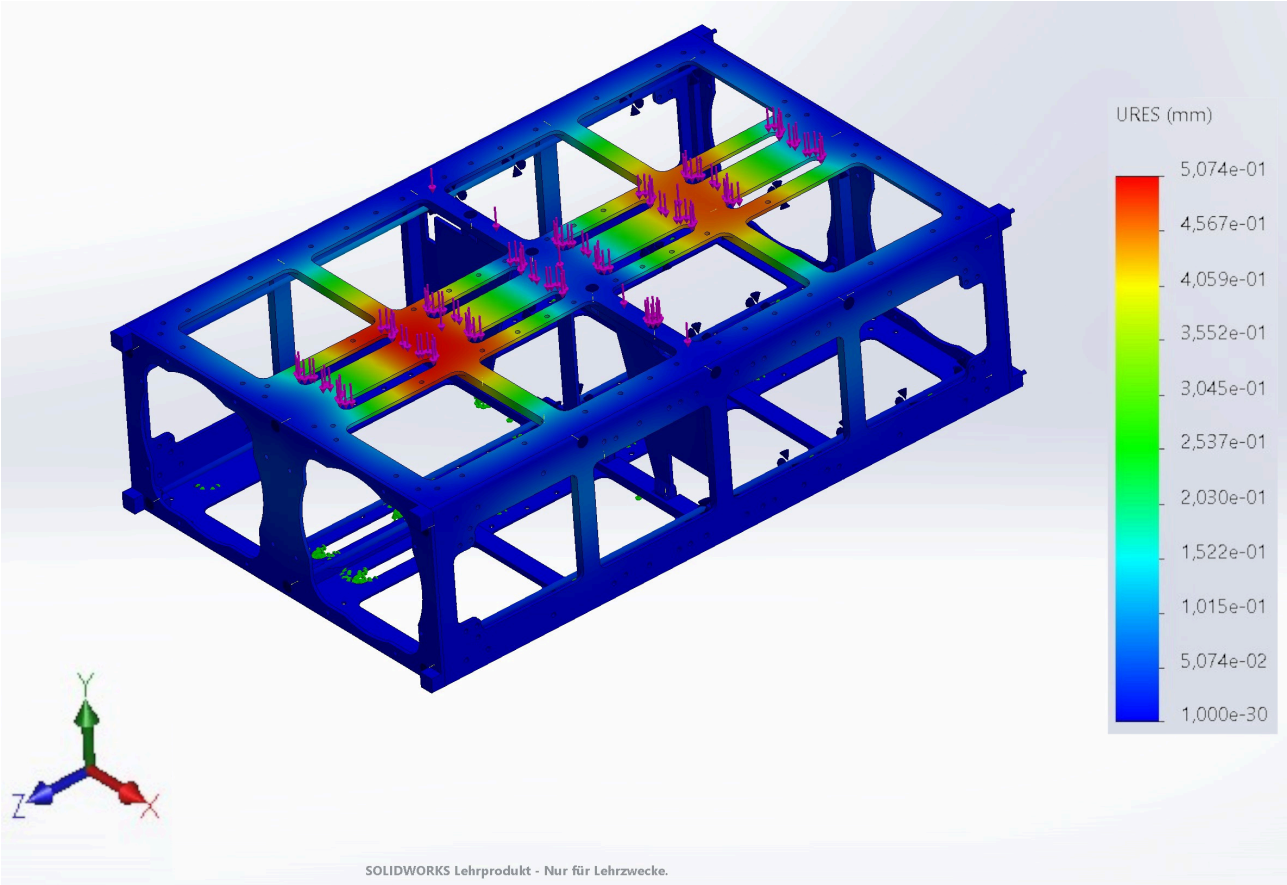

Figure A.6 Displacement results of the static load analysis of the 6U CubeSat structure made out of WE43 micro lattice with a force of 1200N applied in negative Y-direction

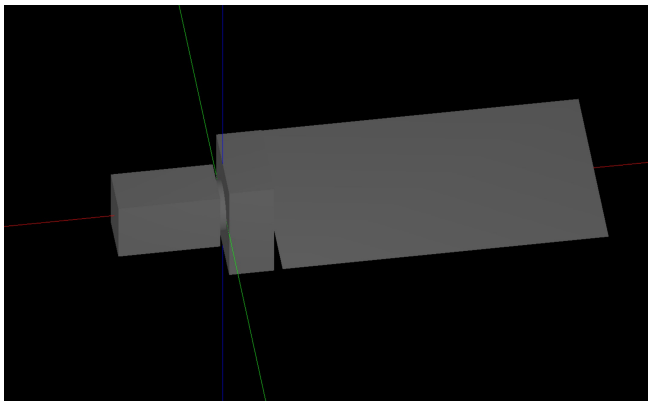

Figure A.7 Standard model of a Satellite in DRAMA

Bibliography

[1] Nesma T. Aboulkhair, Marco Simonelli, Luke Parry, Ian Ashcroft, Christopher Tuck, and Richard Hague. 3d printing of aluminium alloys: Additive manufacturing of aluminium alloys using selective laser melting. *Progress in Materials Science*, 106:100578, 2019.

[2] Fred McMullen Alethia Renee Young. Gsfc-hdbk-8007 mission success handbook for cubesat missions, 2019. Retrieved March 8, 2024.

[3] Daniel Baier, Franz Wolf, Tobias Weckenmann, Maja Lehmann, and Michael F. Zaeh. Thermal process monitoring and control for a near-net-shape wire and arc additive manufacturing. *Production Engineering*, 16(6):811–822, 2022.

[4] J.J. Bertin. *Hypersonic Aerodynamics*. AIAA Education Series, 1994.

[5] V.S. Deshpande, M.F. Ashby, and N.A. Fleck. Foam topology: bending versus stretching dominated architectures. *Acta Materialia*, 49(6):1035–1040, 2001.

[6] ENDUROSAT. Endurosat online shop. Retrieved March 24, 2024, from `https://www.endurosat.com/products/`.

[7] Chris Chikadibia Esionwu. Cubesat market analysis and cost breakdown. 2014.

[8] United Nations Office for Outer Space Affairs. Space debris mitigation guidelines of the committee on the peaceful uses of outer space. In *International Space Law*, pages 89–93. United Nations, 2018.

[9] U.S. Government. U.s. government orbital debris mitigation standard practices, november 2019 update. In *U.S. Government Orbital Debris Mitigation Standard Practices, November 2019 Update*, pages 1–8. U.S. Government, 2019.

[10] Lilith Grassi. Design for demise techniques for medium/large leo satellites reentry. volume 7. ESA Space Debris Office, 2017.

[11] ESA Space Debris Mitigation Working Group. Esa space debris mitigation requirements. pages 1–57. European Space Agency, 2023.

[12] Klaus Hannemann and Longo José. *Handbuch der Raumfahrttechnik*. Carl HANSER Verlag München, 2019.

[13] E. H. Hirschel. *Basics of Aerodynamics*. Springer, 2004.

[14] Matweb. Retrieved March 14, 2024, from `https://www.matweb.com/index.aspx`.

[15] Holden Hyer, Le Zhou, Qingyang Liu, Dazhong Wu, Shutao Song, Yuanli Bai, Brandon McWilliams, Kyu Cho, and Yongho Sohn. High strength we43 microlattice structures additively manufactured by laser powder bed fusion. *Materialia*, 16:101067, 2021.

[16] Battelle Memorial Institute. *Metallic Materials Properties Development and Standardization (MMPDS-17)*. Battelle Memorial Institute, 2022.

[17] Alicia Johnstone. Cubesat design specification. In *CubeSat Design Specification*, pages 1–34. 2022.

[18] Rakeshkumar Karunakaran, Sam Ortgies, Ali Tamayol, Florin Bobaru, and Michael P. Sealy. Additive manufacturing of magnesium alloys. *Bioactive Materials*, 5(1):44–54, 2020.

[19] J.Gilbert Kaufmann. Aluminum alloy database, 2015. https://app.knovel.com/kn/resources/kpAAD00001/toc?filter=table.

[20] D. J. Kessler and B. G. Cour-Palais. Collision frequency of artificial satellites: The creation of a debris belt. *Journal of Geophysical Research: Space Physics*, 83(A6):2637–2646, 1978.

[21] A. Deborah Kramer. *Encyclopedia of Chemical Technology*, volume 15. Kirk-Othmer, 2010.

[22] Mercelis-P. Van Vaerenbergh J. Froyen L. Kruth, J. and M. Rombouts. Binding mechanisms in selective laser sintering and selective laser melting. *Rapid Prototyping Journal*, 11(1):26–36, 2005.

[23] Roland Lagier. *Ariane 5 User's Manual*. arianespace, 2016. Retrieved October 22, 2023, from https://www.arianespace.com/wp-content/uploads/2011/07/Ariane5_Users-Manual_October2016.pdf.

[24] MakeItFrom. 6082-t6 aluminum. Retrieved March 14, 2024, from https://www.makeitfrom.com/material-properties/6082-T6-Aluminum.

[25] Armen Poghosyan and Alessandro Golkar. Cubesat evolution: Analyzing cubesat capabilities for conducting science missions. *Progress in Aerospace Sciences*, 88:59–83, 2017.

[26] J. Puig-Suari, C. Turner, and R. J. Twiggs. Cubesat: The development and launch support infrastructure for eighteen different satellite customers on one launch. 2001.

[27] Alessandro Rossi, Camilla Colombo, Kleomenis Tsiganis, James Beck, Jonathan Becedas Rodriguez, Scott Walker, Federico Letterio, Florio Dalla Vedova, Volker Schaus, Rada Popova, Alessandro Francesconi, Hedley Stokes, Thorn Schleutker, Elisa Maria Alessi, Giulia Schettino, Ioannis Gkolias, Despoina K. Skoulidou, Ian Holbrough, Franco Bernelli Zazzera, Enrico Stoll, and Youngkyu Kim. Redshift: A global approach to space debris mitigation. *Aerospace*, 5(2), 2018.

[28] SatCatalog. Cubesat launch costs. https://www.satcatalog.com/insights/cubesat-launch-costs/#:~:text=The%20cost%20for%20CubeSat%20deployment,for%20deployment%20and%20mission%20operations, 2022, December 10.

[29] Bo Song, Lei Zhang, and Yusheng Shi. Chapter 6 - microlattice metamaterials. In Bo Song, Aiguo Zhao, Lei Zhang, Pengfei Wang, Xiaobo Wang, and Yusheng Shi, editors, *Metamaterial Design and Additive Manufacturing*, 3D Printing Technology Series, pages 223–266. Academic Press, 2023.

[30] SpaceX. Spacex smallsat rideshare program, 2024. Retrieved March 28, 2024, from https://www.spacex.com/rideshare/.

[31] Dassault Systems. Maximum von mises stress criterion. Retrieved March 21, 2024, from https://help.solidworks.com/2022/English/SolidWorks/cworks/r_Maximum_von_Mises_Stress_Criterion.htm.

[32] Dassault Systems. Strain components. Retrieved March 21, 2024, fromhttps://help.solidworks.com/2024/English/SolidWorks/cworks/r_Maximum_von_Mises_Stress_Criterion.htm?verRedirect=1.

[33] G. Sánchez-Arriaga, J.R. Sanmartín, and E.C. Lorenzini. Comparison of technologies for deorbiting spacecraft from low-earth-orbit at end of mission. *Acta Astronautica*, 138:536–542, 2017. The Fifth International Conference on Tethers in Space.

[34] Qiyang Tan, Yu Yin, Ning Mo, Mingxing Zhang, and Andrej Atrens. Recent understanding of the oxidation and burning of magnesium alloys. *Surface Innovations*, 7(2):71–92, 2019.

[35] Y. S. Touloukian, D. P. DeWitt, and Hernicz. *Thermophysical Properties of Matter - The TPRC Data Series. Volume 9. Thermal Radiative Properties - Coatings*. THERMOPHYSICAL AND ELECTRONIC PROPERTIES INFORMATION ANALYSIS CENTER LAFAYETTE IN, 1972.

[36] Ulrich Walter. *Astronautics*. Springer Cham, 2019.

[37] Tetsuo Yasaka and Junjiro Onoda. Spacecraft structures. In Robert A. Meyers, editor, *Encyclopedia of Physical Science and Technology (Third Edition)*, pages 449–461. Academic Press, New York, third edition edition, 2003.

[38] Bruce Yost and Sasha Weston. State-of-the-art amall spacecraft technology. 2024.